DISSERTATIONES
PHYSICAE
UNIVERSITATIS
TARTUENSIS
118

MIKK VAHTRUS

Structure-dependent mechanical properties of individual one-dimensional metal-oxide nanostructures

DISSERTATIONES PHYSICAE UNIVERSITATIS TARTUENSIS
118

DISSERTATIONES PHYSICAE UNIVERSITATIS TARTUENSIS
118

MIKK VAHTRUS

Structure-dependent mechanical properties of individual one-dimensional metal-oxide nanostructures

UNIVERSITY OF TARTU
Press

Institute of Physics, Department of Material Science, Faculty of Science and Technology, University of Tartu.

The dissertation was admitted on 18.12.2018 in partial fulfillment of the requirements for the degree of Doctor of Philosophy in Physics, and was allowed for defense by the Council of the Institute of Physics, University of Tartu.

Supervisor: Prof. Ergo Nõmmiste, Institute of Physics, University of Tartu
Dr. Sergei Vlassov, Institute of Physics, University of Tartu

Opponents: Prof. Irina Hussainova, TalTech
Prof. Alexey Romanov, ITMO University

Defense: February 21, 2019, at the University of Tartu, Tartu, Estonia

This work has been partially supported by Graduate School of Functional materials and technologies receiving funding from the European Regional Development Fund in University of Tartu, Estonia.

ISSN 1406-0647
ISBN 978-9949-77-968-0 (print)
ISBN 978-9949-77-969-7 (pdf)

University of Tartu Press
www.tyk.ee

CONTENTS

LIST OF ORIGINAL PUBLICATIONS

I. **Vahtrus, Mikk**; Šutka, Andris; Vlassov, Sergei; Šutka, Anna; Polyakov, Boris; Saar, Rando; Dorogin, Leonid; Lõhmus, Rünno (2015). Mechanical characterization of TiO_2 nanofibers produced by different electrospinning techniques. Materials Characterization, 100, 98–103.

II. **Vahtrus, Mikk**; Umalas, Madis; Polyakov, Boris; Dorogin, Leonid; Saar, Rando; Tamme, Maret; Saal, Kristjan; Lõhmus, Rünno; Vlassov, Sergei (2015). Mechanical and structural characterization of gamma- and alpha-alumina nanofibers. Materials Characterization, 107, 119–124.

III. **Vahtrus, Mikk**; Šutka, Andris; Polyakov, Boris; Oras, Sven; Antsov, Mikk; Doebelin, Nicola; Lõhmus, Rünno; Nõmmiste, Ergo; Vlassov, Sergei (2016). Effect of cobalt doping on the mechanical properties of ZnO nanowires. Materials Characterization, 121, 40–47.

IV. Vlassov, Sergei; Polyakov, Boris; **Vahtrus, Mikk**; Mets, Magnus; Antsov, Mikk; Oras, Sven; Tarre, Aivar; Arroval, Tõnis; Lõhmus, Rünno; Aarik, Jaan (2017). Enhanced flexibility and electron beam-controlled shape recovery in alumina-coated Au and Ag core-shell nanowires. Nanotechnology, 28 (50), 505707.

Author's contribution

Paper I: The author is responsible for all of the mechanical measurements and composition of the manuscript.

Paper II and III: The author is responsible for SEM characterization, the mechanical measurements, all of the data processing and composition of the manuscript.

Paper IV: The author is responsible for SEM characterization, measurements of mechanical properties and participated in preparation of the manuscript.

PUBLICATIONS NOT INCLUDED IN THESIS

I. Vlassov, Sergei; Polyakov, Boris; Dorogin, Leonid; **Vahtrus, Mikk**; Mets, Magnus; Antsov, Mikk; Saar, Rando; Romanov, Alexey; Lõhmus, Ants; Lõhmus, Rünno (2014). Shape restoration effect in Ag-SiO_2 core-shell nanowires. Nano Letters, 14 (9), 5201–5205.

II. Polyakov, Boris; Antsov, Mikk; Vlassov, Sergei; Dorogin, Leonid; **Vahtrus, Mikk**; Zabels, Roberts; Lange, Sven; Lõhmus, Rünno (2014). Mechanical properties of sol-gel derived SiO_2 nanotubes. Beilstein Journal of Nanotechnology, 5, 1808–1814.

III. Antsov, Mikk; Dorogin, Leonid; Vlassov, Sergei; Polyakov, Boris; **Vahtrus, Mikk**; Mougin, Karine; Lõhmus, Rünno; Kink, Ilmar (2014). Analysis of static friction and elastic forces in a nanowire bent on a flat surface: a comparative study. Tribology International, 72, 31–34.

IV. Vlassov, Sergei; Polyakov, Boris; Oras, Sven; **Vahtrus, Mikk**; Antsov, Mikk; Šutka, Andris, Smits, Kristjanis; Dorogin, Leonid; Lõhmus, Rünno (2016). Complex tribomechanical characterization of ZnO nanowires: nanomanipulation supported by FEM simulations. Nanotechnology, 27 (33), 335701.

V. **Vahtrus, Mikk**; Oras, Sven; Antsov, Mikk; Reedo, Valter; Mäeorg, Uno; Lõhmus, Ants; Saal, Kristjan; Lõhmus, Rünno (2017). Mechanical and thermal properties of epoxy composite thermal insulators filled with silica aerogel and hollow glass microspheres. Proceedings of Estonian Academy of Science, 66 (4), 339–346.

VI. Kruusma, Jaanus; Tõnisoo, Arvo; Pärna, Rainer; Nõmmiste, Ergo; **Vahtrus, Mikk**; Siinor, Liis; Tallo, Indrek; Romann, Tavo; Lust, Enn (2017). Influence of iodide ions concentration on the stability of 1-ethyl-3-methylimidazolium tetrafluoroborate | molybdenum carbide derived carbon electrode interface. Journal of The Electrochemical Society, 164, A1110-A1119.

ABBREVIATIONS

1D MONS	one-dimensional metal-oxide nanostructures
AFM	atomic force microscopy
ALD	atomic layer deposition
EB	electron beam
FEM	finite element method
FIB	focused ion beam
MEMS	microelectromechanical systems
NF	nanofiber
NW	nanowire
SEM	scanning electron microscopy
TEM	transmission electron microscopy
QTF	quarts tuning fork
XRD	X-ray diffraction

PREFACE

Global demand for more powerful and versatile technologies has driven the research for novel materials with superior properties and diverse functionality. Nanotechnology provides the most promising solution as it has been shown that nanostructured materials possess new and improved material properties. In addition, low dimensional nanostructures have the advantages of being much smaller than building blocks of conventional devices.

Among various nanostructured materials, one-dimensional metal-oxide nanostructures (1D MONS) have shown potential in wide range of applications, due to their unique structure and many advantageous properties. Moreover, the properties of 1D MONS can be easily controlled for example by tuning their size, geometry, crystal phase, crystalline size, surface structure and aspect ratio. In applications, the 1D MONS are expected to be identical in shape, uniform in size, perfect in crystalline structure and with repeatable properties. However, achieving this goal remains a challenge. The situation is more complicated since the factors affecting the properties of 1D MONS have not been thoroughly investigated.

In most applications, knowledge of the mechanical properties of 1D MONS is crucial. At the same time, the mechanical properties are highly dependent on the structure of 1D MONS. Therefore, mechanical properties of 1D MONS could be affected for example by the synthesis process, thermal treatment, presence of defects and extra coating. In order to determine the relationship between the structure and mechanical properties thorough characterization must be conducted. Due to the size of 1D MONS, measurement of their properties is a challenging task and many factors must be considered to obtain reliable results.

In the present thesis, systematic structural and mechanical characterization was carried out on 1D MONS. Several aspects that could affect the structure and lead to change in mechanical properties of 1D MONS were studied separately. Great care was taken to eliminate any other factors, e.g. synthesis parameters or mechanical characterization methods, in order to understand the underlying mechanisms. Materials were selected with potential application in mind. Electron microscopy, X-ray diffraction and Raman spectroscopy were used for detailed structural study of different 1D MONS. Mechanical characterization was performed using bending tests carried out either inside scanning electron microscope or with atomic force microscope.

The current thesis is divided into four distinct chapters. In the first chapter, overview of 1D nanostructures, with the emphasis on metal-oxide materials, is given. The main structural and mechanical characterization methods of 1D MONS are described. In addition, detailed analysis of potential factors related to the structure of 1D MONS, which could affect the mechanical properties, are discussed. In the second chapter, aims of the current study are defined. Experimental equipment and procedures used are described in the third chapter. Finally, the results of the experiments are presented and discussed in the fourth chapter. Each factor is presented in separate subsection.

1. BACKGROUND

1.1. One-dimensional metal-oxide nanostructures

1.1.1. One-dimensional nanostructures

Nanostructured (NS) materials are usually categorized by their morphology into four distinct groups – 0 dimensional (0D), 1D, 2D and 3D. The number indicates, how many dimensions of the material are larger than 100 nm. At the same time, some of the characteristic material properties start to change when the size of the object is reduced under 1 μm (so called size effect). Therefore, more general definition of the size of NS material is as follows: NS materials are materials which characteristic properties start to significantly change when their dimensions are reduced under 1 μm.[1]

Compared to other low dimensional NS, 1D NS materials have attracted the most interest due to their unique morphology and fascinating properties [2]. 1D NS can be synthesized in form of rods, wires, needles, tubes, belts, cables, ribbons, fibers and many more. 1D NS have two quantum-confined directions but one unconfined available for electrical conduction [3]. In addition, having one dimension in scale of micrometers up to millimeters allows 1D NS contact the macroscopic world for many physical measurements [2]. Furthermore, 1D NS can be used for bottom-up approach to create nanostructures for nano-science investigation and for nanotechnology application.

The structure and morphology of 1D NS are directly related to their fascinating properties [3]. Due to unique density of electronic states 1D NS are expected to exhibit significantly different optical, electrical and magnetic properties. In addition, increased surface area and surface to bulk atom ratio, defect concentration and distribution, diameter-dependent bandgap, increased surface scattering for electrons and phonons are just some of the reasons why 1D NS differ from their corresponding bulk materials. At the same time, 1D NS are large enough to possess local crystal structures that are closely related to their bulk counterparts, allowing for theoretical prediction about their properties to be made. [3]

1.1.2. One-dimensional metal-oxide nanostructures

Among various materials, metal-oxides (MO) have attracted much research interest over the past few decades [2]. MO are ionic compounds that are composed of positive metallic and negative oxygen ions and the electrostatic interaction between the two results in solid ionic bond. The s-shells of metal-oxides are completely filled but their d-shells may be incomplete. This means that although most MO have good thermal and chemical stability, incomplete d-shells give them variety of unique properties. Characteristic properties of MO include wide bandgap [4], high dielectric constant [5], reactive electronic transition [6], good electrical [7] and optical characteristics as well as super-

conductivity [8]. Therefore, MO are one of the most fascinating functional materials and have been widely exploited in various technological applications [2].

Properties of MO are even more enhanced in 1D form, making 1D metal-oxide nanostructures (MONS) suitable for wide range of applications such as biosensors [9], gas sensors [10], smart windows [11], solar cells [12], photo-catalyst [13], supercapacitors, photodetectors [14], diodes [15] and transistors [16]. Ideally, the 1D MONS used for these applications are expected to be identical in shape, uniform in size, perfect in crystalline structure with low defect concentration and a consistent chemical composition [2]. However, development of synthesis method of 1D MONS for controllable shape, size, crystalline structure and chemical composition remains a challenge.

A number of synthesis methods for 1D MONS have been developed to achieve the goal of identical shape, uniform size, perfect crystal, defect free and homogenous stoichiometry structured materials [2]. Synthesis techniques can be divided into two distinct groups – direct physical deposition and direct chemical deposition techniques. The direct physical techniques include thermal evaporation [17], template-assisted growth [18] and lithography methods [19]. Chemical vapor deposition [20], sol-gel [21] and solvothermal [22] techniques are most common direct chemical deposition methods for synthesis of 1D MONS. The growth mechanisms of 1D MONS involve physical or chemical reaction, nucleation, assembly and crystallization. Various 1D MONS have been successfully synthesized, such as zinc- (Zn), titanium- (Ti), aluminum- (Al), nickel-, copper-, tungsten-, tin-, bismuth-, vanadium-, and molybdenum oxide [2].

Zinc oxide (ZnO) can be synthesized with the molecular formulas of ZnO and ZnO_2 and with two crystal phases – hexagonal and cubic crystals [23,24]. The crystal structure of ZnO may possess wurtzite, zinc-blende and rock-salt form. Under ambient conditions, hexagonal wurtzite structure is the most stable form of ZnO. Due to the noncentral symmetry of wurtzite structure ZnO possesses remarkable piezoelectrical properties. In addition, ZnO has a wide band gap of 3.37 eV, is transparent to visible light, can be made highly conductive by doping, is biosafe and biocompatible [25]. Therefore, 1D ZnO NS have potential applications in a number of industries including opto-electronics, photonics, actuators, and solar cells [26].

Titanium oxides can be found in numerous chemical forms of Ti_nO_{2n-1} and most common is titanium dioxide (TiO_2) [2]. There are many different crystalline phases for titanium oxides, including tetragonal, orthorhombic, monoclinic, hexagonal, triclinic and rhombohedral. TiO_2 may possess rutile (tetragonal), anatase (tetragonal) and brookite (orthorhombic) crystalline structure. The TiO_2 structure is composed of octahedral with shared oxygen atoms. The neighboring rutile octahedra shares corners along the [110] direction while the anatase phase shares along the (001) plane. 1D TiO_2 NS have excellent photocatalytic properties, large specific surface area, are stable and easy to synthesis. Therefore, TiO_2 can be used for photocatalytic degradation of pollutants, water splitting, solar cells, supercapacitors, lithium-ion batteries, filtration and gas sensors [27].

Alumina oxide can be synthesized in various forms, most common is Al_2O_3 (alumina) [28]. Alumina can be found in hexagonal α, cubic γ and η, monoclinic θ, hexagonal χ, orthorhombic κ and δ crystalline phase. Most common phase is α-Al_2O_3 (corundum), where oxygen cations nearly form a hexagonal closed-packed structure and the aluminium anions fill two-thirds of the octahedral sites. The stable phase of alumina has high strength, high elastic modulus, high melting temperature and is chemically stable [29]. Favorable properties of alumina allow them to be potentially used as catalysts, microelectronics, reinforcing components, optics, fire protection, and energy storage [30].

1.2. Structural characterization of one-dimensional metal-oxide nanostructures

Characteristic sizes of 1D MONS are less than half the wavelength of visible light which makes it impossible to see the morphology and the structure using traditional optical microscopy [2]. Therefore, the primary tools for structural characterization of nanostructured materials are electron microscopy, X-ray diffraction (XRD) and Raman spectroscopy [2,31–34]. Obtained results help to understand the relationship between the mechanical and structural properties and allow to associate the variation in mechanical properties to change in the structure of 1D MONS.

Two main methods of electron microscopy are the scanning electron microscopy (SEM) and transmission electron microscopy (TEM) [31]. SEM enables for fast visualization of the 1D MONS and allows to determine their size, shape, uniformity and distribution but lacks atomic resolution and no information about the interior of the sample can be obtained. TEM gives further information about the morphology of the 1D MONS and enables to study their inner structure, e.g. uniformity of crystal structure, nanocrystalline size, atomic spacing, size and angel of grain boundaries, presents of defects and contamination layers and thickness of layers. At the same time, sample preparation for TEM measurements is time consuming and requires substantial skill.

XRD is based on the interference of X-rays that are reflected from the atomic planes of a crystal governed by the Braggs law [35]. XRD is the most convenient method to examine the crystal structure of 1D MONS. X-rays are relatively easily generated, and a large variety of techniques have been developed for measurement and subsequent data analysis. For example, XRD allows to extract information about the crystal structure, crystalline phase transition, unite cell parameters, crystalline size and internal stresses.

Single-crystal XRD methods cannot be used in case of 1D MONS as it is impossible to conduct measurements on a nanosized single test object using conventional measurement equipment [35]. Therefore, powder XRD is mainly used. Powder XRD measures the diffraction pattern of the powder made from individual 1D MONS and allows for representation of the overall properties of the material. As the powder sample is randomly oriented, every plane of the

crystal structure will be oriented so that interference condition is satisfied. Therefore, each crystal plane is represented in the obtained diffraction pattern. Advantages of powder XRD further include simple sample preparation, non-destructive analysis and fast measuring process.

In addition to XRD measurements Raman spectroscopy can be used to gather information about the crystal structure of 1D MONS [31]. Raman spectroscopy relies on the analysis of inelastic scattering of monochromatic light which is characteristic to the studied crystal structure.

1.3. Mechanical characterization of individual one-dimensional metal-oxide nanostructures

1.3.1. Methods

Tensile test

Tensile test is one of the most common techniques used for mechanical characterization of individual 1D MONS [36–42]. Experimental configuration of tensile test is as follows: object under testing is fixed at both ends and is deformed by applying uniaxial load. During the tensile test, load and the strain are simultaneously measured. Knowing the exact cross-section of the test object, stress-strain curve is obtained, and the Young's modulus can be calculated from the linear part of the curve. Tensile test also enables to calculate the ultimate tensile strength and toughness for oxide materials.

There are two main methods to conduct tensile test on 1D MONS. The first approach involves a nanomanipulation setup inside a SEM and using an AFM cantilever as a force sensor (Figure 1) [38,39,41]. One end of the test specimen is attached to the force sensing cantilever and the other end to a nano-manipulator tip or a second stiff AFM cantilever. The test specimen is fixed either by focused ion beam (FIB) or electron beam (EB) induced deposition. Deformation of the 1D MONS is determined from SEM images, applied force is calculated using the deformation and spring constant of the AFM cantilever.

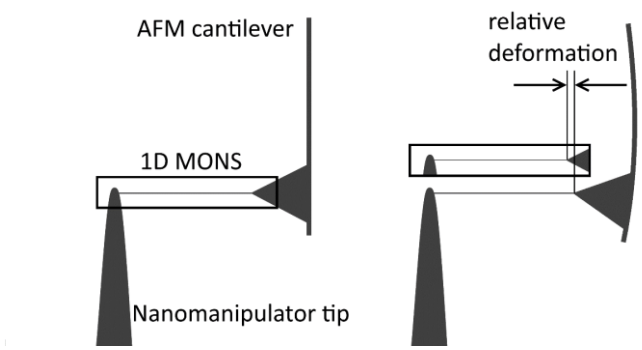

Figure 1. Tensile test of 1D MONS using AFM cantilever and nanomanipulator tip.

Second method relies on specific home-made microelectromechanical systems (MEMS) [36,37,40,42]. In MEMS setup thermal, piezoelectric or electrostatic actuators and sensors are used to apply uniaxial force and measure the strain. Nanomanipulators are used to position the 1D MONS to the test beds and again FIB or EB induced deposition is used to fix the test specimens in place. Usually, such system requires prior calibration and is used inside electron microscope to allow visual feedback of the nanomanipulation process.

Bending test

Bending test is relatively simple method for mechanical characterization of 1D MONS [43–49]. Method relies on the bending of test specimen that is fixed at least at one end and with some part freely suspended. During the bending process deflection and applied force is measured. Here, AFM cantilever is the most used force sensor. Knowing the cross-section and dimensions of the test specimen, elastic beam theory is applied to extract the Young's modulus values. Bending strength values can be calculated when the tested material is bent until breaking. Bending test can be conducted both inside electron microscope or AFM as direct visualization is not necessary required.

Bending test can be divided into two distinct methods based on the measurement configuration. When the 1D MONS is fixed at one end and the other end is freely suspended, term cantilever beam bending is used (Figure 2c,-d) [43–45]. Test specimens are usually dispersed from solution onto a patterned substrate with periodical holes or groves [44,47–49]. Sometimes nano-manipulation [43] or vertically grown test specimens [45] are used. Mainly AFM calibration grids or TEM grids are employed as patterned substrates. In case of a test object fixed at both ends and suspended over an opening three-point bending scheme is used (Figure 2a,-b) [46–49]. Three-point bending can be performed in lateral [47,49] or vertical mode [46,48]. In lateral mode, test specimen is dragged laterally at the midpoint, simultaneously measuring applied force and displacement. In vertical mode, suspended sample is pushed at the middle. In both configurations FIB or EB deposition is used to fix the 1D MONS when adhesion between the test specimen and substrate is not sufficient enough.

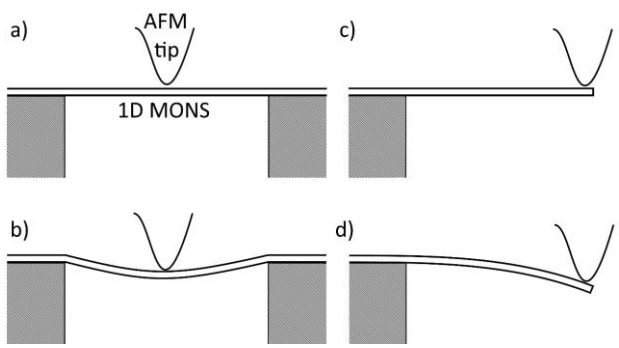

Figure 2. Three-point bending (a,b) and cantilever beam bending (c,d) scheme.

Nanoindentation test

Nanoindentation can be considered the most convenient method for characterization of 1D MONS due to the simple sample preparation and fast measurement procedure [50–52]. Test samples are deposited on a flat and hard surface and a sharp tip is used to ident the sample (Figure 3a,-b). AFM is a perfect tool to conduct nanoindentation measurements due to the small size of AFM cantilever tip and capability to measure force-distance curve (Figure 3c). Mechanical properties are calculated from applied load (F), indention depth (δ) and tip properties. Hertz model describes the relationship between the elastic modulus (E) and force-displacement curve values through the following equation:

$$F = \frac{4}{3} E^* R^{\frac{1}{2}} \delta^{\frac{3}{2}} \quad \textbf{(1)}$$

where R is the tip radius of AFM cantilever and E^* is the reduced Young's modulus which is related to the Young's modulus of tested specimen by:

$$\frac{1}{E^*} = \frac{1 - \upsilon_{TS}^2}{E_{TS}} + \frac{1 - \upsilon_{CT}^2}{E_{CT}} \quad \textbf{(2)}$$

where E_{TS} and υ_{TS} are the Young's modulus and Poisson's ratio of the 1D MONS and E_{CT} and υ_{CT} are the same quantities for the cantilever tip, respectively [53]. Therefore, special care must be taken when selecting indention tip as too soft AFM tip will be deformed when pressing into hard oxide material which in turn may lead to a significant error in the results.

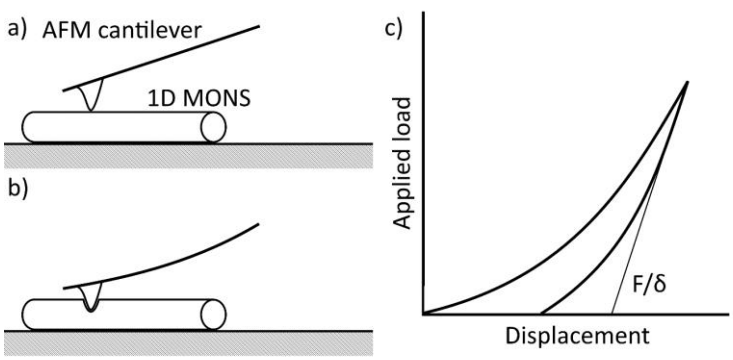

Figure 3. Nanoindentation of 1D MONS using AFM cantilever (a, b) and the corresponding force-displacement curve.

Resonance test

Another established method for mechanical characterization of individual 1D MONS is resonance test [54–56]. In the resonance test, mechanical oscillations are induced in a single freestanding test specimen and the natural resonance frequency is found. Young's modulus (E) is calculated from the resonance frequency (f) using the following equation:

$$f = \frac{\beta_i^2}{2\pi L^2}\sqrt{\frac{EI}{m}} \quad \textbf{(3)}$$

where L is the length of the freestanding part, I the area moment of inertia and m the unit length mass of the test specimen. β_i is a constant for the ith harmonic, values of the first two harmonics are β_1=1.875 and β_2=4.694.

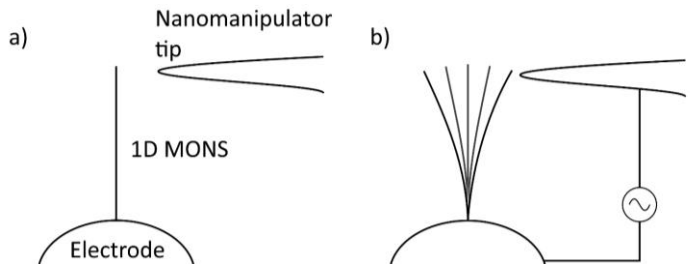

Figure 4. Resonance test of 1D MONS using two electrodes.

1D MONS can be exited directly on the substrate, where they were grown or picked up and attached to a probe using FIB or EB induced deposition. Oscillation of the test specimen can be produced by two methods. First method uses two electrodes – test specimen is located on one electrode and second electrode is attached to nanomanipulator allowing to approach the specimen (Figure 4a) and to induce resonance [54,55]. Alternating voltage is applied between two electrodes and frequency is changed until mechanical resonance is induced in the test specimen (Figure 4b). Second method involves attachment of the test specimen to a probe which in turn is glued to a piezoelectric sheet [56]. Mechanical resonance is induced by applying alternative voltage to the piezo-electric sheet. As resonance test requires real-time visual observation to detect resonance, measurement is conducted inside electron microscopy.

Buckling test

Experimental setup used for tensile test of 1D MONS can also be applied to conduct buckling test [41,57]. Opposite to tensile test, test specimen is subjected to compressive stresses until a critical buckling force (F_{cr}) is reached. Young's modulus (E) can be calculated using the Euler's formula [58]:

$$F = \frac{n\pi^2 EI}{L^2} \quad \textbf{(4)}$$

where L is the length of the 1D MONS between the fix points and n a constant that is defined by the boundary conditions of the fix test specimen.

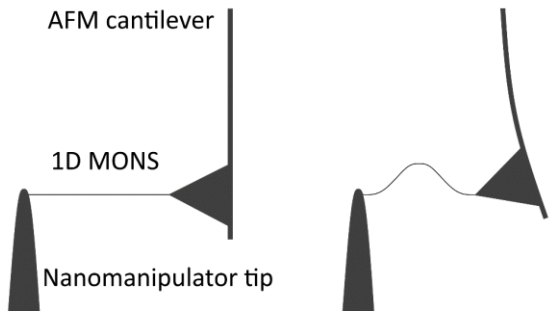

Figure 5. Buckling test scheme using a nanomanipulator tip and AFM cantilever.

Buckling test is carried out inside electron microscope to allow for precise manipulation and visualization. One end of the 1D MONS is fixed to a nano-manipulator and the other end to an AFM cantilever which acts as a force sensor (Figure 5). Nanomanipulator is used to push the test specimen into the AFM cantilever, the deflection of the AFM gives the value of the applied load. Axial compressive loads lead to buckling and subsequent bending of the test specimen until it breaks.

1.3.2. General challenges

The main challenge for mechanical characterization of individual 1D MONS is the small size of the specimen which means that conventional macroscopic test methods cannot be used [59,60]. Due to the size of the test specimen, challenges can be grouped as follows: (1) manipulation and positioning of the specimen for the test; (2) clamping of the specimen; (3) force and deformation detection; (4) visualization of the measurement process.

Almost all of the methods used for mechanical characterization of 1D MONS rely on the manipulation of individual test specimen from synthesis substrate or solution onto the required test bed or configuration [59,60]. Simplest solution is to use substrate with numerus test beds and place a drop of solution containing 1D MONS onto the substrate [44]. The test specimens are randomly distributed and due to the large number of test beds there is a high probability that some specimens are in the suitable configuration. This method works well for bending

test as substrates with holes or groves are easily manufactured. As discussed before, tensile and buckling tests are performed on 1D MONS which are clamped between two probes [38,39,41,47]. Here, nanomanipulators are required to move and place the test specimen in the suitable test bed. Nano-manipulation systems usually consist of nanopositioner with a probe that has a sharp tip. Nanopositioner is based on multiaxial piezo actuators which allow for nanometer precise movement. Nanomanipulation requires direct visual guidance and therefore are conducted inside electron microscopes.

Once the test specimen is in the right configuration for the experiment, next crucial step in the measurement procedure is the clamping of the 1D MONS [59,60]. As boundary condition can play major role in the determination of the mechanical properties, great deal of attention must be paid towards insuring that the test specimens are fully fixed [61]. Primary methods of clamping are FIB [43] and EB [38] deposition, where precursor is decomposed and deposited by the secondary electrodes of the beam. Precursor is usually introduced in gaseous or solid form near the deposition site. FIB deposition rates are higher than EB but FIB deposition suffers from lower spatial resolution and must be used together with SEM.

Mechanical characterization of 1D MONS involves measurement of applied force and subsequent deformation in the nanonewton and nanometer scale, respectively [59,60]. MEMS or AFM cantilevers are mostly used to detect such small forces [36,41]. Fabrication of MEMS-based testing system is a rather complicated task and very accurate calibration procedure is needed for precise force detection [36]. At the same time MEMS can be very versatile tool as it can also be used to measure deformation at high spatial resolution. AFM cantilevers are used either inside AFM, SEM or TEM to measure force during deformation of the 1D MONS [41,47]. For high accuracy, it is crucial to determine the exact value of the cantilever spring constant and to conduct precise calibration. Deformation is measured either using EM images or AFM laser signal.

As mentioned several times before visualization of the measurement is done by either electron microscope or AFM [59,60]. Main advantage of AFM is the fact that no extra nanomanipulation equipment is necessary [47,50]. AFM cantilever acts as a force sensor, nanomanipulator and visualization device. Unfortunately, this means that in AFM these tasks cannot be done simultaneously and important information about the real-time processes during the test are lost. Therefore, electron microscopy is the preferred method meaning that special nanomanipulation setups must be built and placed inside high-vacuum conditions which again gives rise to a number of challenges [36,40]. Nanomanipulation setups inside electron microscopes must be vacuum proof, e.g. materials with low rate of outgassing in order not to contaminate the vacuum chamber and the sample. Setup must be small enough to fit into the electron microscope and all of the wiring must be shielded in order to avoid effecting the electron microscope image.

1.3.3. Source of errors

Large discrepancy in the measured mechanical properties is a characteristic to 1D MONS which can be partly explained by number of errors related to the measurement procedure [36,37,40,43]. Main source of errors includes accuracy and calibration of the force sensor, determination of test specimen dimensions, presence of electron beam (EB), test configuration and method.

MEMS force sensing systems are usually directly calibrated before measurement procedure due to fabrication uncertainties which may result in the actual device dimensions being different from design values [37]. Likewise, AFM cantilevers require calibration and reliable method for determining the normal force constant [62]. There are over dozen different calibration methods, including geometric method, forced and thermal oscillation, static loading and finite element analysis [63]. Different methods can give uncertainty of up to 40% in normal force constant values [63]. Therefore, initial mistake in calibration procedure or choice of calibration method can lead to substantial errors in calculation of mechanical properties values.

Even higher uncertainty for obtained values can be attributed to errors due to the measurement of 1D MONS dimensions [40]. Equations for Young's modulus calculation include specimen length in second or third power and radius in the fourth power [58,64]. Dimensions are measured using either AFM or electron microscopy, therefore resolution of the measuring device determines directly the accuracy. AFM has a high vertical resolution but suffers from low lateral resolution which is limited by tip radius and wear. Highest measurement accuracy is usually obtained by TEM which at the same time is the most complicated and expensive method. Therefore, SEM with high-resolution (down to 1 nm) is usually used. In addition to radius and diameter, determination of the cross-section is also important. Cross-section of the same 1D MONS material can be for example circular or hexagon or even any arbitrary shape between the two [36,40]. The difference, in calculated area moment of inertia values using either circular or hexagonal cross-section for the same measured diameter, is up to 30% (area moment of inertia of circular and hexagonal cross-section is approximately $0.79r^4$ and $0.54r^4$, respectively). Hence, accurate measurement procedure involves measuring the exact cross-section of the test specimen.

In addition, the effect of EB, which is one of the primary tools for mechanical characterization, must be considered [65–69]. Bombardment of high-energy electrons can lead to the structural change of 1D MONS which consequently effects the mechanical properties. Therefore, values obtained for the same material but measured using different microscopes can vary. Various EB driven effects have been reported in the literature, including enhanced plasticity of amorphous silica [65], increased anelasticity of CuO nanowires [66], EB induced amorphization of SiC nanowires [67], and EB driven phase transition of TiO_2 [68]. Furthermore, EB can cause charging of the substrate, test specimen and/or manipulation probe [69]. This can lead to significant increase of adhesion between test specimen and substrate or repulsion between manipulation probe and specimen.

In turn, this will cause under- or overestimation of the applied force and lead to error in calculation of mechanical properties.

Difference in the test configuration can lead to substantial error in measurement result [70,71]. First, assumption of a perfectly fixed test specimen must be realized in the experiment [70]. Weakly clamped 1D MONS can lead to slipping of the ends and thus to the underestimation of the elastic values. In addition, uncertainty related to the fixed points of the test specimen influences the determination of the clamping length and again leads to an error in the calculation of the elastic values [61]. In the three-point bending configuration, the ratio of the suspension length to the specimen diameter should be relatively large (approximately 20) to decrease uncertainty of the measurement value [61]. Tensile test requires application of uniaxial strain which means that the test specimen must be perfectly aligned [71]. Any deviation from uniaxial configuration may lead to bending and twisting of the test specimen and subsequently cause a significant error in the measurement result.

Finally, the last factor that should be considered as potential source of error is the influence of the test method [38,41]. As discussed before, tensile test involves uniaxial deformation of the 1D MONS and the load is uniformly distributed over the cross-section [40]. Therefore, tensile test is not sensitive to the inhomogeneous nature of 1D MONS which arises from the fact that the surface atoms possess different properties compared to the bulk atoms. Meanwhile non-uniform distribution of defects and surface effects can play a major role in the experiments, where the mechanical properties of 1D MONS are found from bending tests [46,48,49]. Difference in loading modes has led to a distinction between tensile modulus and bending modulus [41]. Main difference between the test methods is that bending test is more sensitive to surface effects and therefore the modulus values can be higher for larger diameter nanowires when compared to values measured by tensile test for the same material [41]. Core-shell model with stiffened shell is used to explain the differences in measured values between the two methods [38,41].

1.4. Influence of structure on the mechanical properties of one-dimensional metal-oxide nanostructure

For macroscale materials, it is very well known how the microstructure defines the mechanical properties of material [72]. Interatomic forces, chemical bond type, strength and direction between atoms, ions and molecules and presents of defects are directly related to the mechanical properties of materials like elasticity, hardness, yield strength, Young's modulus, etc. Same principles can be applied to nanoscale materials, but as mentioned in section 1.1. extended surface and quantum effects make situation more complicated. At the same time, the applicability of 1D MONS strongly depends on the capability of preparing structures with reproducible properties. Therefore, it is of great importance to

investigate the factors that affect the structure and subsequently the mechanical properties of 1D MONS.

In section 1.1.2. it was shown that 1D MONS can be synthesized using several fundamentally different techniques and the same material can be produced with numerous crystal structures. Mechanical properties of the same material with different growth direction or crystalline structure can have very different values. Moreover, just a slight adjustment in growth conditions can result in materials with different mechanical properties [40]. Wang et al synthesized ZnO nanowires using thermal evaporation. Just by changing the gas flow rate they were able to produce nanowires with either circular or hexagonal cross-section. Structural characterization showed no difference in crystal structure and both samples were single crystalline with hexagonal wurtzite structure. At the same time, uniaxial tensile test showed that the Young's modulus of nanowires with circular cross-section were significantly lower than for hexagonal nanowires. Similar studies of 1D MONS produced from the same precursor but using different synthesis process, could expand the understanding of the role of synthesis on the structural and mechanical properties of nano-structures.

Synthesized 1D MONS can be subjected to further thermal treatment (annealing) which for example can be related to specific application, incorporation into composite materials or to improve the mechanical properties. Tan et al studied the effect of annealing on the structural and mechanical properties of electrospun polymeric nanofibers [73]. Electrospun nanofibers were annealed at 75°C which was slightly above the crystallization temperature. The mechanical properties of as-spun and annealed nanofibers were measured using three-point bending test inside AFM. Annealing led to increase of Young's modulus values due to the increase in crystallinity and enhanced intrafibrillar bonding. Further studies on metal-oxide nanostructures with well-defined crystal structure could offer valuable information on the effect of annealing.

Defects play an important role in determining the mechanical properties of 1D NOSM. It is well known that the fracture strength of material is dependent on the number of critical defects [74]. He et al measured the diameter dependence of fracture strength of ZnO nanowires and determined that with the decrease of nanowire diameter the strength was increased [75]. They proposed that this effect was related to point defects (oxygen and zinc ion vacancies) as no structural defects were observed in TEM studies. The decrease of point defect concentration with the decrease in diameter was confirmed by cathodo-luminescence characterization. Point defects can also affect the Young's modulus values. Theoretical [76,77] and experimental [40] studies have shown that increase in point defect (especially vacancies) concentration will lead to change in bond energy and length subsequently decreasing the Young's modulus value of the material. Role of defects could be further investigated by introducing dopants of different material into the nanostructures.

Properties of 1D NS can be efficiently modified and improved by coating them with a thin layer of oxide material, resulting in a core-shell heterostructure

[78,79]. Theoretical studies on core-shell 1D NS have shown that coating can also improve the mechanical properties of materials. Ma et al showed that thickness of thin SiO_2 layer on SiC nanowires can greatly affect the Young's modulus of such core-shell nanowires [80]. Such acute dependence of surface layer has led many authors to develop theoretical core-shell models to explain the size effect of 1D NS [38,41,54]. Here, homogenous nanostructure is divided into core with bulk modulus of the material and shell with effective elastic modulus and thickness of few nanometers. The interplay between the two modulus determines the overall modulus of the nanostructure. When coating is involved in creating core-shell 1D NS, the interface between the core and shell material plays an important role. It has been shown that the interface may significantly influence the overall plastic response of a core-shell nanowire during loading [81] and different strains in the interface can lead to non-linear dependence of Young's modulus on the composition of the core and the shell [82]. Unfortunately, there are only few experimental works available on metal-oxide core-shell nanostructures. Therefore, addition studies are required to understand the effect of oxide coating on 1D NS.

2. AIMS OF THE STUDY

The main goal of the present study was to expand the fundamental understanding of the relationship between the mechanical properties of one-dimensional metal-oxide nanostructures and crucial technological parameters like method of synthesis, presence of dopants, and thermal treatment. In order to achieve this goal number of objectives were set and detailed structural characterization and complex nanomanipulation experiments for mechanical characterization were conducted on different materials. List of main objectives was as follows:

- Assessment of synthesis process influence on the structure and the mechanical properties of TiO_2 nanofibers.
- Effect of annealing on the structural and the mechanical properties of Al_2O_3 nanofibers.
- Doping effect on the structural and the mechanical properties ZnO nano-wires.
- Determination of the effect of Al_2O_3 coating on the mechanical properties of metal nanowires.

3. EXPERIMENTAL

3.1. Structural characterization of one-dimensional metal-oxide nanostructures

In the present study, structural characterization of 1D MONS was carried out by electron microscopy, X-ray diffraction (XRD) and Raman spectroscopy. Two different high-resolution scanning electron microscopes (HR-SEMs) were mainly used to measure the size, shape, uniformity and distribution of 1D MONS. Helios Nanolab 600 (*FEI*) SEM had a resolution of 0.9 nm and was equipped with focused ion beam source and energy-dispersive X-ray spectroscope. Nova NanoSEM 450 (*FEI*) SEM had a resolution limit of 1.4 nm and could be used in low-vacuum mode. In addition, Tecnai GF20 (*FEI*) transmission electron microscope (TEM) with line resolution of 0.12 nm was applied for the inner structure studies of 1D MONS. 180 kV accelerating voltage was used for imaging the characterization of 1D MONS.

Powder XRD was used to determine the crystal structure of 1D MONS. Two different X-ray diffractometers were used – Ultima+ (*Rigaku*) and D8 Advanced (*Bruker*). For Ultimate+ CuKα radiation at wavelength of 1.5406 Å was used at room temperature. Powder XRD patterns were recorded at 2θ from 10° to 80°. Scanning rate was set 1° min^{-1} and diffraction pattern was recorded with a step width of 0.01°. D8 Advanced diffractometer used digitally and Ni-filtered CuKα radiation. Diffraction pattern was scanned at 2θ from 8° to 100° with resolution of 0.0122° and counting time of 0.15 s per step. Results of the powder XRD measurement were compared against diffraction patterns in the crystallography open database and the crystal structure was determined. In case of D8 Advanced further analysis was conducted. The diffraction patterns were evaluated by Rietveld refinement and Le Bail profile fitting with the software Profex [83] and the Rietveld refinement kernel BGMN [84]. This allowed to determine the cell parameters of the structure and evaluate the crystallite sizes and internal strain.

Finally, InVia (*Renishaw*) Raman microscope was used for Raman spectroscopy. Samples were excited by a 514 nm laser directly through an upright DM LM (*Leica*) microscope's objective lens. Backscattered light spectrum was collected by InVia spectroscope in the same optical path as the incident laser beam. Spectroscope had a grating of 1800 groves/mm and spectral resolution of approximately 0.5 cm^{-1}.

3.2. Mechanical characterization of one-dimensional metal-oxide nanostructures

Mechanical characterization of 1D MONS was carried out by using two distinct methods – cantilever beam bending and three-point bending. Two different nanomanipulation setups were developed for Young's modulus and bending

strength measurement using cantilever beam bending method inside SEM. Both cantilever beam bending and three-point bending techniques were used inside an AFM to determine Young's modulus. SEM-based methods allowed for direct observation of the nanomanipulation process including actual contact point between probe and individual 1D MONS at every stage of bending test, the corresponding profile of the tested object, crack formation and propagation, as well as close-up inspection of the freshly fractured area in vacuum. AFM enabled a simple setup for nanomanipulation experiments with high force resolution and precise measurement of 1D MONS down to 10–20 nm in diameter.

3.2.1. Cantilever beam bending inside SEM

Cantilever beam bending technique is based on bending of a beam with a uniform cross-section that is clamped at one end and free at the other end [64]. When a point force (F) is loaded at the free end of the beam with the suspension length of l, behavior of the beam under bending is described by elastic beam theory as follows:

$$EI\frac{d^2\theta}{dl^2} + Fcos\theta = 0 \quad \textbf{(5)}$$

where E is the Young's modulus of the beam, I the area moment of inertia and θ is the angle between the tangent of the bent profile and the initial straight profile.

Area moment of inertia for circular, pentagonal and hexagonal cross-section are as follows:

$$I_{circ} = \frac{\pi r^4}{4} \quad \textbf{(6)}$$

$$I_{pent} = \frac{1}{6}\frac{(3-\sqrt{5})}{(3+\sqrt{5})}\sqrt{256+118\sqrt{5}}r^4 \quad \textbf{(7)}$$

$$I_{hex} = \frac{5\sqrt{3}}{16}r^4 \quad \textbf{(8)}$$

where r is the (apparent) radius of the beam.

Cantilever beam bending was also used to determine the bending strength of the 1D MONS. Bending strength is the maximum stress that a beam can withstand before fracture. In the cantilever beam bending configuration the maximum stress (σ_{max}) is given by:

$$\sigma_{max} = Er\kappa \quad \textbf{(9)}$$

where κ is the curvature of the beam just before breaking.

3.2.1.1. Young's modulus

Young's modulus measurements were carried out inside Vega-II SBU (*TESCAN*) SEM using a home-made nanomanipulation setup (Figure 6) [85]. Quartz tuning fork (QTF, *ELFA*) with resonance frequency of 32.768 kHz was used as a force sensor (Figure 6b). QTF is a perfect tool for nanoscale force sensing as the resonance frequency of the QTF is highly sensitive to the force acting on the crystal [86]. AFM cantilever was glued to one of the prongs of the QTF to allow manipulation of single 1D MONS (Figure 6c). In turn, QTF was attached to 3D piezo nanopositioner (SLC-1720-S, *SmarAct*) which allowed precise movement of the force sensor (Figure 6a). Nanopositioner has two distinct working modes – fine and coarse. Fine mode is based on expansion and contraction of the piezo element which allows for precise moment of the nanopositioner from few nanometers up to 1.5 μm. In coarse mode movement is achieved by series of gradual expansions of piezo element followed by abrupt slips achieved via sawtooth signal sent to the element. This allows to move the nanopositioner up to 12 mm in all three directions. QTF oscillation was excited by applying alternating voltage using a lock-in amplifier (SR830, *Stanford Research System*) and recorded by analog-digital converter (NI PCI-6036E, *National Instruments*). QTF was excited in shear mode meaning the AFM cantilever attached to the prong was oscillating parallel to the plain of bending/ substrate surface.

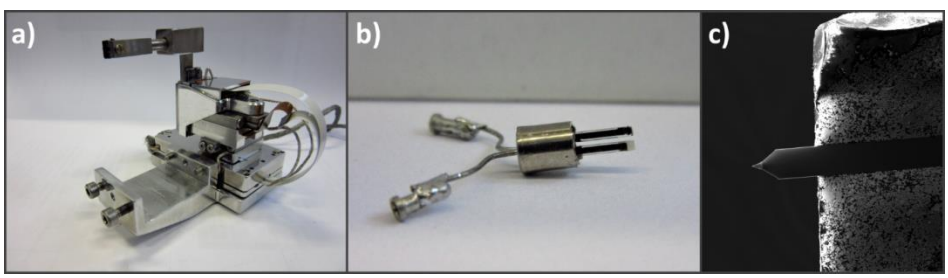

Figure 6. Home-made nanomanipulation setup: SmarAct nanopositioner (a), QTF (b) with electrical contacts and AFM cantilever glued to the end of one of the prongs (c).

QTF isn't direct force measurement method as only change in resonance frequency is obtained from the bending experiment. Calculation of the loading force applied during the experiment required further calibration of the force sensor. Precalibrated AFM cantilever with spring constant of 0.056 N/m was

used to obtain force values. During the calibration process force sensor was used to bend the AFM cantilever and simultaneously resonance amplitude signal was recorded. Using the spring constant of the AFM cantilever relationship between the amplitude and the force was determined for the force sensor. From this, force applied during the experiment was calculated.

Prior to Young's modulus measurements radius and the suspension length of suitable 1D MONS were measured inside one of the HR-SEM described in section 3.1.1. Next, the sample was placed inside TESCAN SEM and Young's modulus measurements were conducted by in-plane bending of the 1D MONS using the nanomanipulation setup described previously. Video of the SEM images of the bending experiment was simultaneously recorded. Young's modulus was calculated by numerically fitting actual bent profile of the 1D MONS from experiment with equation (5) using corresponding force sensor value, suspension length and radius of the test object. Numerical fitting was performed for different degrees of bending to obtain the most reliable result.

3.2.1.2. Bending strength

Bending strength measurements were performed inside Helios HR-SEM using commercially available nanopositioner (MM3A-EM, *Kleindiek*). Nanomanipulation system inside HR-SEM lacked force sensing capability but allowed for more accurate imaging of the bending process, crack formation and breaking of the 1D MONS. Kleindiek nanopositioner works in polar coordinate system and composes of three piezoelements. Corse mode allows for working range of 100 cm^3 and fine mode sub-nanometer resolution. Again, AFM cantilever (ATEC-CONT) was attached to home-made probe holder of the nanopositioner to allow bending of individual 1D MONS.

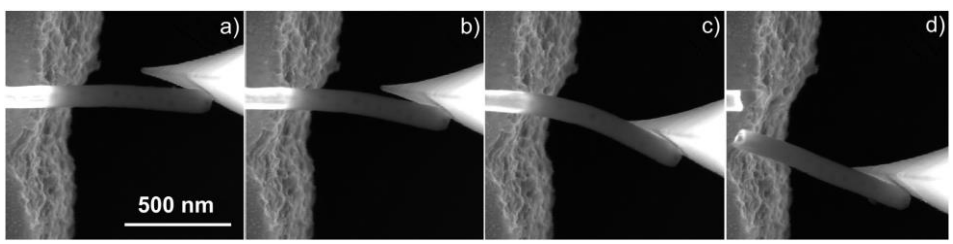

Figure 7. Bending strength measurement of Al_2O_3 nanofibers using AFM cantilever. Curvature just before breaking (c) is used to calculate the value [87].

During bending strength experiment, first HR-SEM image of suitable 1D MONS was recorded which allowed to measure the radius and the suspended length of the test object. Next, 1D MONS was gradually bent using fine mode of nanomanipulator until the test object broke (Figure 7). Simultaneously, series

of SEM images or video was recorded of the bending experiment. Bending strength values were calculated using equation (9). Curvature of the 1D MONS was obtained from the SEM images just before the breaking (Figure 7c) and the Young's modulus value obtained from previous measurements was used.

3.2.1.3. Fatigue

In addition to bending strength measurements, Kleindiek nanopositioner allows for fatigue measurements of 1D MONS using the oscillation mode. Both the amplitude and the frequency of the oscillation can be changed to suite the measurement. Experiment was performed by first making a contact between the test object and tip of the nanomanipulator and then the oscillation mode was turned on. Next, oscillation amplitude was increased until the 1D MONS was bent close to the yield point. Amplitude of the oscillation was measured from the HR-SEM images. Fatigue test was performed up to 1 million cycles or until the test object broke.

3.2.1.4. Weibull statistics

Weibull statistics was implemented to quantitively compare uniformity of mechanical properties of 1D MONS [74,88]. The method is widely used for representation of material's strength distribution which is usually governed by the statistical distribution of critical defects. Weibull statistics give the cumulative probability distribution of fractures P_S at the maximum bending stress (bending strength) σ_{max} for a sample as follows:

$$P_S = 1 - \exp[-\left(\frac{\sigma_{max}}{\sigma_0}\right)^m] \quad \textbf{(10)}$$

where σ_0 is the bending strength at which 63% of the samples will break. m is the Weibull modulus which is a dimensionless parameter used to describe variation in the measured strength values. Higher m value corresponds to a steeper slope in the Weibull plot and indicates lower deviation in the bending strength values.

3.2.2. Bending methods inside AFM

Young's modulus calculation using three-point bending method inside AFM is based on elastic beam theory [89]. In three-point bending configuration, elastic beam is fixed at both ends and suspended over an opening (Figure 8a). If a point force F is applied at the middle of the beam (length L) the force-displacement relationship is as follows:

$$F = \frac{192IE}{L^3}\delta \tag{11}$$

where E is the Young's modulus, I is the area moment of inertia and δ displacement of the beam at the middle. In terms of Young's modulus:

$$E = \frac{k_B L^3}{192I} \tag{12}$$

where $k_B=F/\delta$ is the stiffness of the beam. This relationship is true only for linear elastic regime and small displacements. If we also consider the tensile strain of the beam then the Young's modulus can be found by [90]:

$$E = \frac{k_B L^3}{192I(1 + \frac{A}{24I}\delta^2)} \tag{13}$$

where A is the cross-section area of the beam.

For cantilever beam bending configuration the force-displacement relationship becomes much simpler and is given by the following equation:

$$E = \frac{k_B L^3}{3I}\delta \tag{14}$$

AFM-based Young's modulus measurements were performed by Dimension Edge AFM (*Bruker*) under ambient conditions using tapping-mode cantilevers (PPP-NCHR, *Nanosensors*). First, HR-SEM was used to select and measure the radius and suspensions length of suitable 1D MONS either in three-point bending or cantilevered beam bending configuration. Series of SEM images with different magnifications were taken which allowed to locate the selected 1D MONS in AFM. Built-in optical microscope was used to move the tip of the AFM to right location and then a low magnification (usually 10x10 μm) images were taken to ensure proper tip position. Next, higher magnification (between 1x1 μm to 3x3 μm, depending on the size of the test object) images of the suitable 1D MONS were recorded. Tip of the AFM cantilever was placed approximately at the center or at the end of the 1D MONS for either three-point bending or cantilever beam bending configuration, respectively. Several force-displacement curves were taken at different displacements using built-in software. The extent of the displacement depended on diameter and suspension length of the test object.

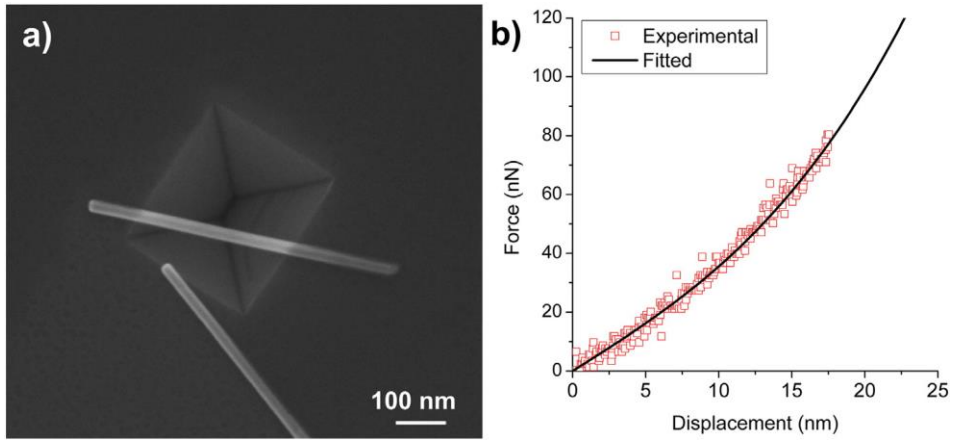

Figure 8. SEM images of ZnO nanowire in three-point bending configuration (a) and the decoupled force-displacement curve obtained by AFM (b) [91].

Raw AFM data of the built-in software contained only the z-position (in nm) of the AFM cantilever holder and relative change of the laser signal (in volts) reflected from the tip to the photodiode. Calibration of the AFM cantilever, which consisted of determining sensitivity and normal force constant of the cantilever, was required to obtain real force-displacement values (Figure 8b). Sensitivity of the cantilever, e.g. how large deflection of the cantilever (in nm) produces a drop of 1 V of laser signal, was obtained by measuring force-displacement curve on a hard surface, where indentation of the tip into the material can be neglected. Sensitivity was used to decouple raw AFM data into the corresponding deformation of the AFM cantilever and the test object. Normal force constant of the cantilever used in the measurement was calculated using the geometry of the cantilever measured by HR-SEM [62]. Forced applied during the bending experiment was calculated from the normal force constant and deformation of the AFM cantilever. Elastic regime, e.g. liner part of the force-displacement curve, was taken into account for Young's modulus calculations. Values obtained in the experiments were inserted into equations (13) or (14) to obtain Young's modulus values.

3.2.3. Sample preparation

Mechanical characterization of individual 1D MONS using different bending methods requires structured substrate with grooves and holes. In the present study two different patterned substrates were used – TEM grids (1500 mesh copper grid, *Agar Scientific*, Figure 9a,-b) and silicon substrates with inverse pyramids (Figure 9c,-d). Silicon substrates were prepared by nanosphere lithography [92]. No additional steps were made to fix 1D MONS to the substrate since the

adhesion between two interfaces was sufficient to prevent any slipping [92]. Ultrasonic treatment was used to break up and disperse the 1D MONS in the solution. Drop-casting was used to place samples from solution onto the patterned substrates.

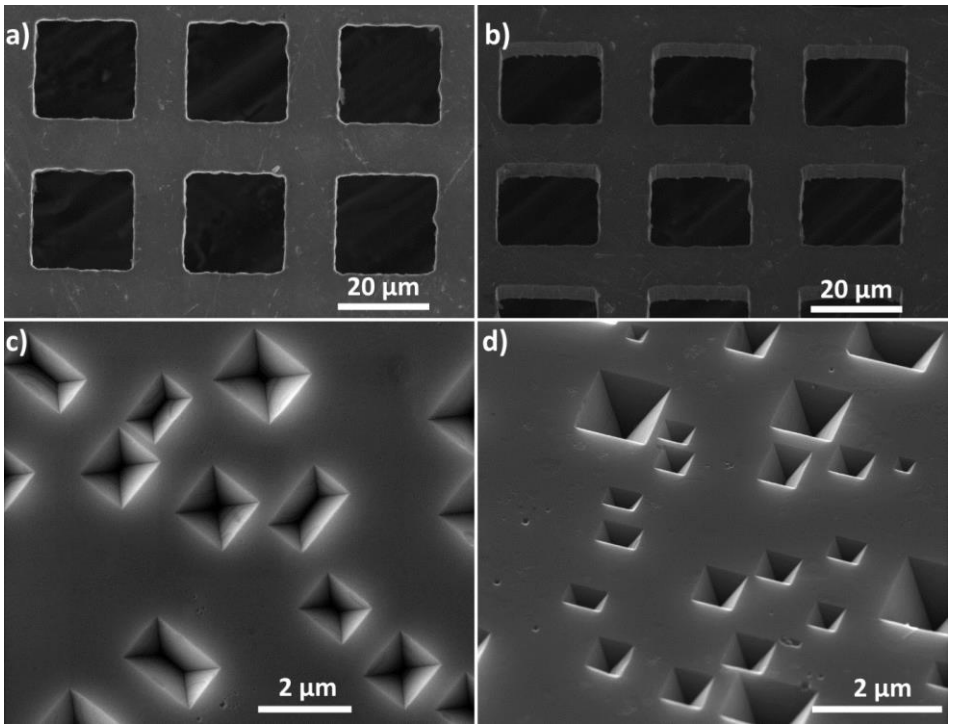

Figure 9. TEM grid (a-b) and silicon substrate with inverted pyramids (c-d).

4. RESULTS AND DISCUSSION

4.1. Synthesis process influence on the mechanical properties of TiO_2 nanofibers (publication I)

Aim of this section was to find out if the same synthesis methods with two different approaches could produce materials with comparable structural and mechanical properties. For this purpose, TiO_2 nanofibers (NFs) were produced by needle and needleless electrospinning process. Needle electrospinning method is a laboratory scale process, which suffers from low production rate, while needleless electrospinning is more suitable for industrial scale production [93]. Both techniques are characterized by high degree of control over the spinning condition. The same precursor was used for two electrospinning processes to exclude any other factor that could influence the properties of the TiO_2 NFs. Structural and mechanical properties were characterized using Raman spectroscopy, XRD, TEM, SEM and in situ SEM nanomechanical testing.

4.1.1. Preparation of TiO_2 nanofibers

Precursor of TiO_2 for electrospinning methods were made by mixing 0.64 ml of titanium tetraisopropoxide with 1.2 ml of acetic acid and 1.2 ml of absolute ethanol and then stirred for 1 h. Final mixture was obtained by adding the solution to 3 ml of absolute ethanol that contained 0.18 g of polyvinyl-pyrrolidone. Needle electrospinning process was conducted by home-made setup using 23-gauge stainless steel needle connected to a high-voltage power supply (LNC 30000-2pos, *Heinzinger*). The feeding rate 1 µl/min for the solution was controlled with a syringe pump (Multi-Phaser NE-500, *New Era*). Electrospinning was conducted in ambient air atmosphere using aluminum foil as collector substrate placed 15 cm from the needle tip. In needleless electrospinning process TiO_2 NF mats were produced by commercially available electrospinning equipment (Nanospider Lab 200, *Elmarco*). Synthesis was performed at room temperature using pike spinning electrode with diameter of 1 cm and length of 15 cm. DC voltage during electrospinning was varied from 65 to 70 kV. For both techniques obtained nanofiber mats were dried at room temperature in ambient atmosphere for 12 h and then annealed at 500°C for 3 h.

4.1.2. Structural properties of electrospun TiO_2 nanofibers

Crystal phase of nanofibers were characterized by powder XRD and Raman analysis described in detail in section 3.1. Raman spectra of annealed electrospun NFs (Figure 10a) produced by two techniques revealed six characteristic Raman-active modes $A_{1g}+2B_{1g}+3E_g$ corresponding to anatase phase [94] with following allowed bands: 144 cm^{-1} (E_g), 197 cm^{-1} (E_g), 399 cm^{-1} (B_{1g}), 513 cm^{-1}

(A_{1g}), 519 cm^{-1} (B_{1g}) and 639 cm^{-1} (E_g). Anatase crystal structure was also clearly demonstrated on the powder XRD spectra (Figure 10b) collected by Ultima+ diffractometer.

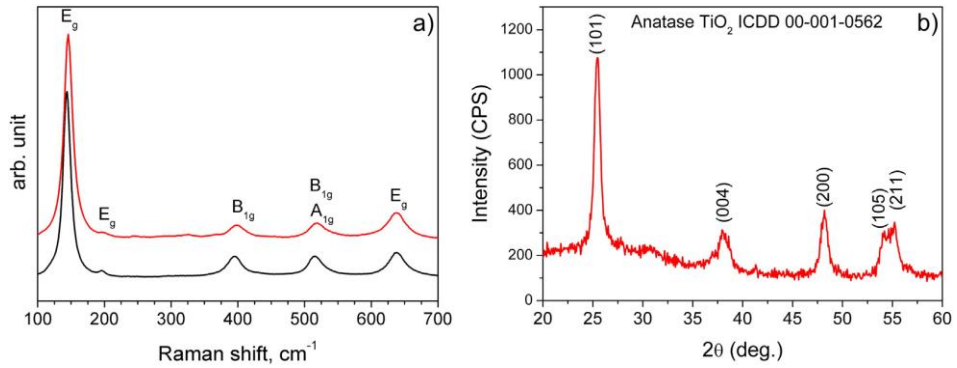

Figure 10. The Raman spectrum of anatase TiO_2 electrospun NFs obtained by needle (black line) and needleless (red line) electrospinning process (a). The powder XRD pattern of the electrospun NFs produced by needle electrospinning (b).

Nova HR-SEM was used to determine the size and morphology of the electrospun TiO_2 NFs. Both electrospinning techniques yielded uniform bead-free nanofibers. On average, needle electrospinning process produced NFs with larger diameter (median value of 129 nm) compared to needleless electrospinning (median 103 nm). TEM inspection of individual TiO_2 NFs revealed polycrystalline morphology and absence of internal defects like voids and cracks (Figure 11). NFs consisted of randomly oriented nanocrystals with size in range of 10–30 nm.

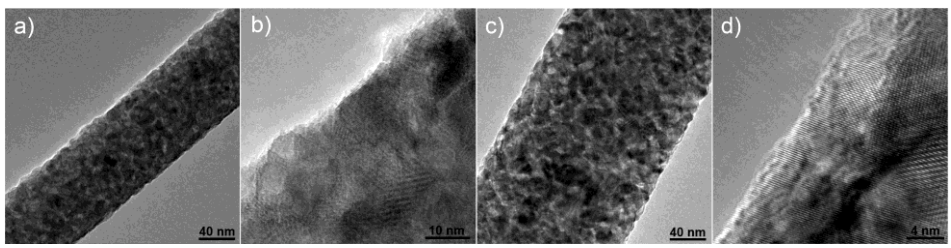

Figure 11. TEM images of TiO_2 NFs produced by needle (a-b) and needless (c-d) technique.

4.1.3. Mechanical characterization of electrospun TiO2 nanofibers

Mechanical characterization electrospun TiO_2 NFs was carried out by cantilever beam bending method inside SEM described in section 3.2.1. Individual test samples were obtained by placing electrospun TiO_2 NF mats in ethanol and treated for 3 h in ultrasonic bath. TEM grids were used as suitable substrates for all the mechanical experiments. Young's modulus measurements were carried out on 10 needle and 17 needleless electrospun TiO_2 NFs with radius between 101 to 223.5 nm and suspended length of few micrometers. Measurement results are depicted in Figure 12. Median Young's modulus values of two different samples were found to be 92±12 GPa and 95±19 GPa for the needle and needleless techniques, respectively. Thus, both electrospinning techniques produce NFs with nearly the same elastic properties. Obtained results are considerably higher than previously reported values [95–97]. Higher values of Young's modulus can be explained by difference in synthesis methods and conditions that may result in TiO_2 NFs with different microstructure. In particular, our NFs may have higher density (less pores and inner voids) due to probably better conditions for solvent evaporation, longer annealing time and higher temperature and less impurities.

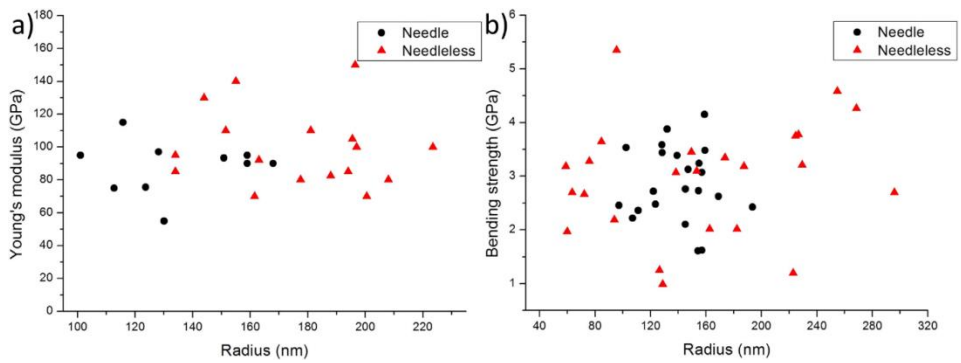

Figure 12. Young's modulus (a) and bending strength (b) values versus radius of needle and needleless electrospun TiO_2 NFs.

Bending strength tests were performed on 22 needle and 24 needleless TiO_2 NFs with radius between 58.9 and 295.9 nm. Bending strength was determined by Eq. (9) using median Young's modulus value presented before. Median bending strength for needle and needleless electrospun TiO_2 NFs was found to be 2.7±0.8 GPa and 3.1±0.6 GPa, respectively (Figure 12b). Obtained results again indicate that both electrospinning techniques produce nanofibers with very similar mechanical properties. It can be seen from Figure 12b that bending strength values are considerably more scattered in comparison to Young's modulus values. This

situation is typical for nanostructures since in contrast to Young's modulus, strength is usually determined by the presence of the critical structural defects [79]. Distribution of defects in nanostructures is non-uniform and can vary from NF to NF. Median bending strength found in our experiments is significantly higher than 1.4 GPa measured previously by tensile test [95]. This is expectable since in tensile test strain uniformly is distributed along the fiber and therefore probability of the presence of the critical defect is higher than in bending test, where critical defects should be in close proximity to the most strained area.

Finally, Weibull statistics discussed in section 3.2.1.4 was implemented to quantitatively compare uniformity of the bending strength values of TiO_2 NFs. Using Eq. (10) Weibull probability distribution was plotted, and Weibull modulus extracted. Modulus values of 4.55 and 2.75 for needle and needless electrospun TiO_2 NFs were found, respectively. This result suggests TiO_2 NFs produced by needle electrospinning are more uniform in microstructure and mechanical behavior. Difference in mechanical behavior may be attributed to the micro-structural peculiarities (surface defects, cracks and pores) which may arise due to the fact that solution jets are generated from open solution surface in needleless electrospinning, as well as peculiarities of the electrospinning technological equipment (electrode), the applied voltage and the spinning direction [98].

4.2. Effect of annealing on the crystal structure and mechanical properties of Al_2O_3 nanofibers (publication II)

In this section effect of annealing on the crystal structure and mechanical properties of Al_2O_3 NFs were investigated. Commercially available alumina NFs were characterized before and after annealing at 1400°C. This temperature is common sintering temperature required for densification of ceramics [99] and was chosen since one of the most promising application of alumina NFs is being reinforcement material in ceramic matrix compounds [100]. Structural characterization of alumina NFs was carried out by SEM, TEM and powder XRD, mechanical properties were obtained from SEM-based nanomanipulation experiments.

4.2.1. Preparation of alumina nanofiber samples

The Al_2O_3 NFs were purchased from *MemPro Ceramics* and had diameter between few tens to few hundreds of nanometers (average 156 nm) and lengths over 100 μm. NF mats were annealed at 1400°C in air for 1 h using an alumina tube furnace (HTRH, *Nabertherm*). Individual test specimens were obtained by placing very low concentration (0.3 mg/ml) of NF mats in isopropyl alcohol and then sonicating them for 45–100 min in an ultrasonic bath. Drop of the solution was placed on TEM grids for mechanical characterization.

4.2.2. Structural characterization of Al_2O_3 nanofibers

Crystalline structure of Al_2O_3 NFs was determined using powder XRD and the patterns were collected by Ultima+ diffractometer. The XRD patterns of the untreated and annealed alumina NFs are presented in Figure 13. All of the broad diffraction peaks of the untreated NFs (Figure 13b) can be indexed as cubic γ-Al_2O_3 (COD No. 2015530). The XRD pattern of the annealed nanofibers (Figure 13a) shows strong and sharp peaks due to the hexagonal α-Al_2O_3 phase (COD No. 1000032). The XRD analysis indicates that the phase transition of γ-alumina to α-alumina occurs below 1400°C which is consistent with the previously reported results [101,102].

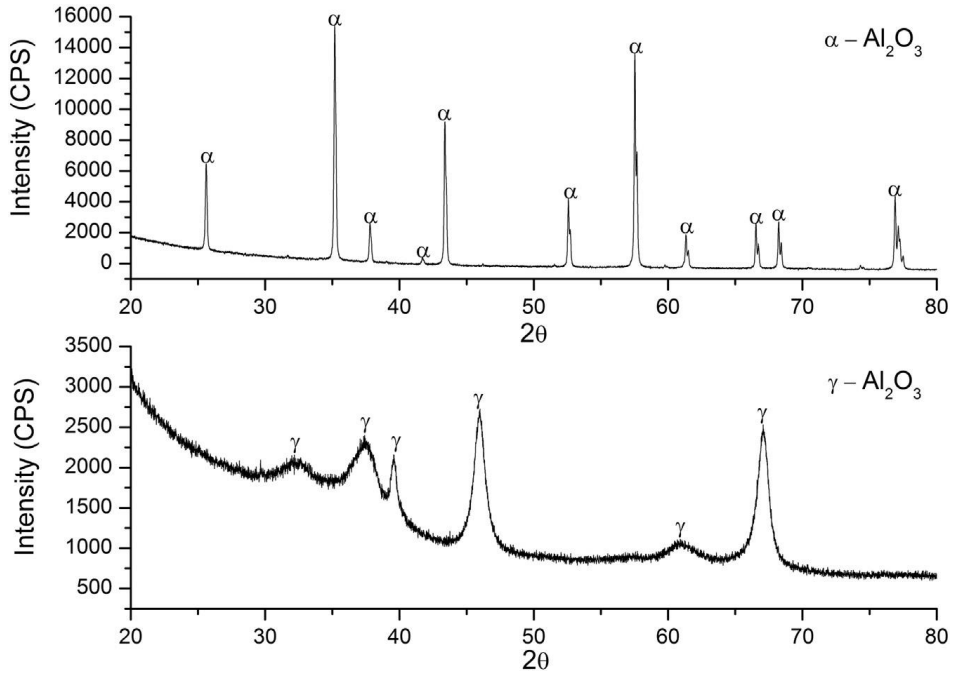

Figure 13. XRD patterns of the α-alumina (a) and the γ-alumina (b) NFs with their characteristic peaks.

Nova HR-SEM inspection of untreated and annealed Al_2O_3 NFs revealed no considerable change in the average diameter between two samples. However, the diameters of the annealed fibers were less uniform. TEM measurements of the untreated alumina NFs (Figure 14a-b) revealed a polycrystalline structure, with nanocrystals in the range of a few nanometers to 20 nm. The annealed NFs exhibited a monocrystalline structure with irregular internal voids (Figure 14c-d). The development of the unusual microstructure during thermal treatment may be ascribed to a change of density which lead to inner strain and the subsequent

formation of voids [103]. Interestingly, even after sonication, some fraction of the annealed Al_2O_3 NFs remained connected in the form of branched structures. Close-up SEM and TEM inspections of intersecting NFs (Figure 15) revealed no boundaries at the junction, indicating complete monocrystalline interfusion caused by annealing. Thinning of the alumina NF was often observed near an intersection which can be explained by the softening of the material and diffusion of the atoms. Although the melting point of *Mempro* alumina NFs is above 2032°C, intersecting NFs were previously demonstrated to soften and form interfiber bonds at lower temperatures starting from approximately 1000°C [104].

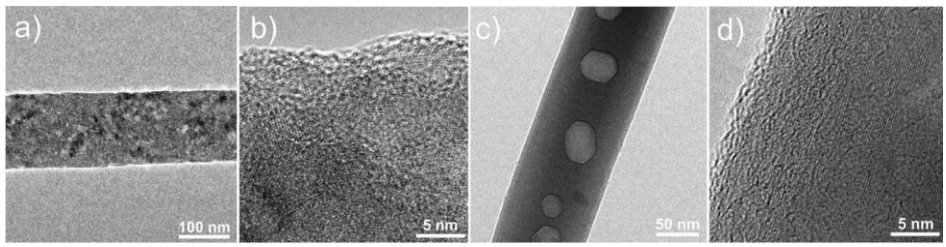

Figure 14. TEM images of the untreated (a-b) and annealed (c-d) alumina nanofibers.

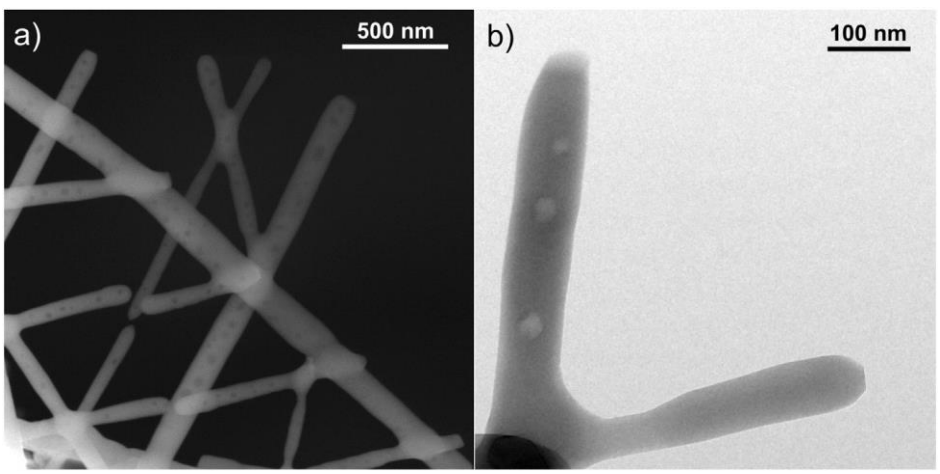

Figure 15. SEM and TEM images of the intersecting annealed Al_2O_3 NFs.

4.2.3. Mechanical characterization of Al_2O_3 nanofibers

Mechanical characterization of untreated and annealed alumina NFs was performed using cantilever beam bending method described in section 3.2.1. Measurements of Young's modulus were conducted on 18 untreated and 12

annealed alumina NFs with radius between 60 nm and 129 nm. The median Young's modulus values were found to be 143±38 GPa and 245±35 GPa for untreated and annealed Al_2O_3 NFs, respectively (Figure 16a). These values are approximately magnitude higher than previously reported values for alumina NFs [105,106]. The results can be explained by the difference in the synthesis methods which resulted in nanofibers with larger diameter and different crystal structure. Moreover, obtained values in this study are much closer to the Young's modulus of bulk alumina (370 GPa). Higher Young's modulus value for annealed NFs is expected as the higher crystallinity of the α-phase leads to improvement in the mechanical properties [73].

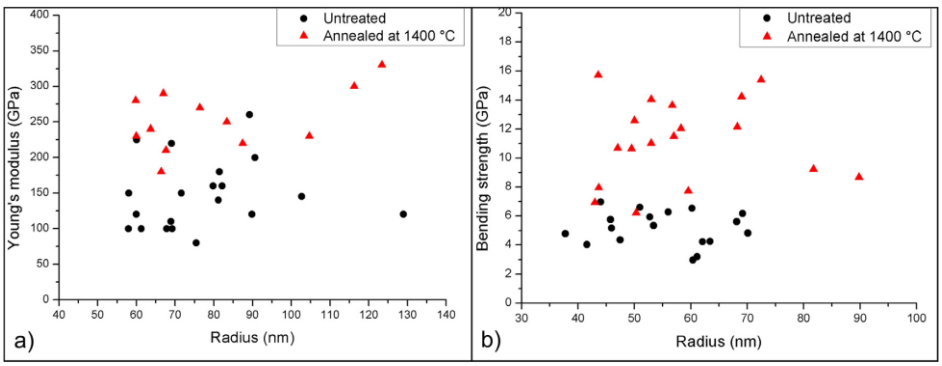

Figure 16. Young's modulus (a) and bending strength (b) values of the untreated and annealed Al_2O_3 nanofibers.

Bending strength tests were performed according to method described in section 3.2.1.2. on 18 untreated and 18 annealed Al_2O_3 NFs with radii between 38 nm to 90 nm. The bending strength values were calculated via Eq. (9) using the previously determined median Young's modulus values and the radius of the nanofiber measured form the HR-SEM image. The median bending strength value for the annealed Al_2O_3 was two-times higher than that for untreated nanofibers: 11.3±2.3 GPa and 5.3±1 GPa for the annealed and untreated cases, respectively (Figure 16b). Bending strength values were again used to calculate Weibull distribution probability and Weibull modulus were extracted. The values of Weibull modulus for untreated and annealed alumina NFs were 4.27 and 3.76, respectively. This result suggests that although annealed Al_2O_3 NFs possessed much higher Young's modulus and bending strength values, there is no considerable difference in the mechanical behavior of the two samples.

Separate bending tests were also conducted on interfused Al_2O_3 NFs. No sliding or breaking at the intersection of the NFs was observed, confirming that the annealed NFs are strongly fused together. In total, 10 alumina NFs protruding from branched structures were tested and a medium bending strength value of 13.1 ± 4.1 GPa was found. This bending strength value is even slightly

higher than the value obtained for individual annealed alumina NFs which can be explained by the higher density of the material near the joint. The entire branched structure demonstrated a dampening effect which undergoes compression or tension as a single NF is bent. Observed behavior indicates that the stresses are delocalized and distributed more evenly, thereby allowing the entire structure to withstand higher loads and deformations.

Finally, fatigue tests were performed on 3 untreated and 3 annelid Al_2O_3 NFs with diameter between 47 to 67 nm according to measurement setup depicted in section 3.2.1.3. The single fatigue test lasted for 17 min with an oscillation frequency of 1000 Hz was used which resulted in more than 1 million bending cycles. All of the tested fibers passed the fatigue test without failure and demonstrated no visible signs of fracture or residual deformation.

4.3. Influence of Co doping on the structural and mechanical properties of ZnO nanowires (publication III)

Goal of the current section was to determine the effect of doping on the structure and mechanical properties of 1D MONS. Zinc oxide (ZnO) nanowires (NWs) were chosen due to the well-defined crystal structure and their remarkable physical properties and numerous promising applications (see section 1.1.2.). In addition, ZnO NWs are one of the most intensively studied nanostructured materials. Physical properties of ZnO can be efficiently modified by doping with transition metals, one of the most suitable dopants being cobalt (Co) [107]. Moderate concentrations of Co does not disturb the growth of ZnO NWs since Co has a similar cation radius to Zn and the same oxidation state resulting in an isovalent substitution of Zn in ZnO lattice [108]. Pure and Co-doped ZnO NWs were grown in similar conditions to exclude any influence of synthesis process on the properties of the NWs. Structural properties of the NWs were characterized by powder XRD, SEM and TEM. The mechanical characterization included three-point bending test made with AFM and cantilever beam bending tests performed inside SEM.

4.3.1. Preparation of ZnO and Co-doped ZnO nanowires

ZnO and Co-doped ZnO NWs were synthesized using solvothermal method by mixing zinc acetate dihydrate $Zn(CH_3CO_2)_2{\cdot}2H_2O$ 0.1 M and 0.5 M NaOH solution in absolute ethanol. For Co-doped NWs a corresponding amount of $Zn(CH_3CO_2)_2{\cdot}2H_2O$ was replaced with $Co(CH_3CO_2)_2{\cdot}4H_2O$ to obtain $Zn_{1-x}Co_xO$, where x=0.025, 0.050, 0.075, 0.100, 0.150 and 0.200. The diameter of the NWs depends on the duration of the solvothermal process, therefore to obtain ZnO NWs with different diameters three different processing times were used: 24 h, 72 h and 150 h. Samples for powder XRD were ground manually in acetone and subsequently dispersed on a zero-background sample holder. Single

NW for mechanical characterization was obtained by sonication in an ultrasonic bath for 5–10 min. The dispersed NWs were then drop-casted onto silicon substrate with inversed pyramids.

4.3.2. Structural characterization of ZnO and Co-doped ZnO nanowires

Crystal structure and unit cell dimensions of ZnO and Co-doped ZnO NWs were determined using D8 Advance diffractometer. All samples were found to contain phase-pure $(Zn_{1-x}Co_x)O$ with XRD peaks positions matching the positions of the zincite reference structure (Figure 17). The incorporation of Co resulted in changes of the relative peak intensities, for example a reduction of the 002 peak at 34.42 °2θ, minor shifts of the diffraction peaks due to the distortions of the unit cell, as well as in the distortions of the peak's shapes. The wurtzite lattice topology was preserved at all Co concentrations and up to 20% of Co could be incorporated in the zincite crystal structure without phase separation. Distorted peak shapes indicated the presence of complex lattice distortions. At 20% Co a drastic loss of XRD peak intensity and increased peaks width illustrated that the crystal growth of the zincite structure was inhibited, resulting in a significant reduction of the mean crystallite size. Le Bail profile (described in section 3.1.) was fitted to determine the unit cell dimensions. Increase of Co concentration led to decrease of c-axis length (from 0.5208 to 0.5202 nm) and increase of a-axis length (from 0.3250 to 0.3256 nm).

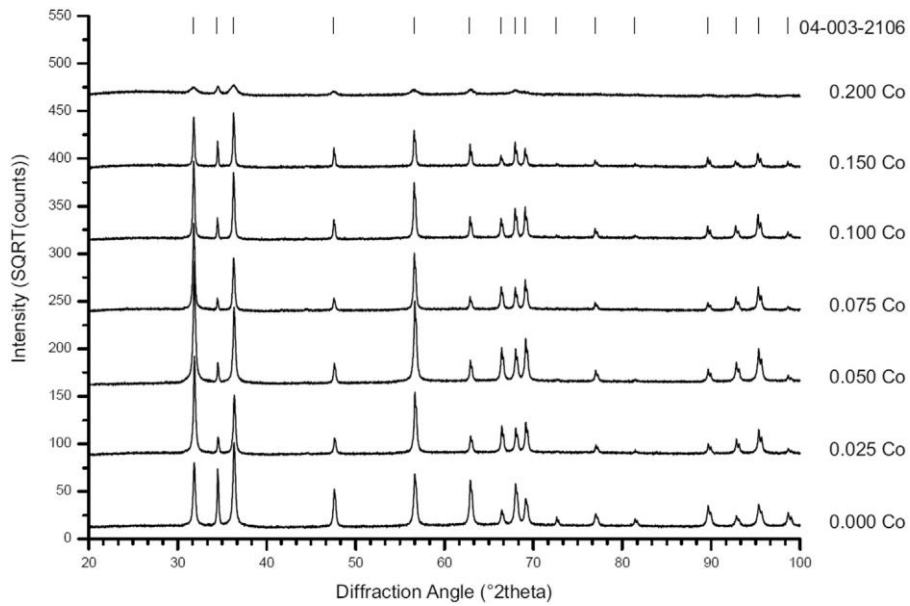

Figure 17. XRD patterns for ZnO NWs with different Co doping percentage.

Helios HR-SEM images of the pure ZnO NWs revealed a uniform morphology, smooth facets and a well-pronounced hexagonal cross-section (Figure 18a) which is typical for wurtzite ZnO grown in [0001] direction. The NW diameters ranged from few tens to few hundreds of nanometers and lengths up to few micrometers. A similar morphology was revealed for Co-doped ZnO NWs with moderate Co doping concentrations (Figure 18b). Starting from 7.5% Co content numerous defects (mostly dislocations) were observed on the surface of NWs and the diameters were less uniform with steep steps (Figure 18c). At even higher Co concentration facets of NWs were less pronounced and cross-section became more rounded (Figure 18d).

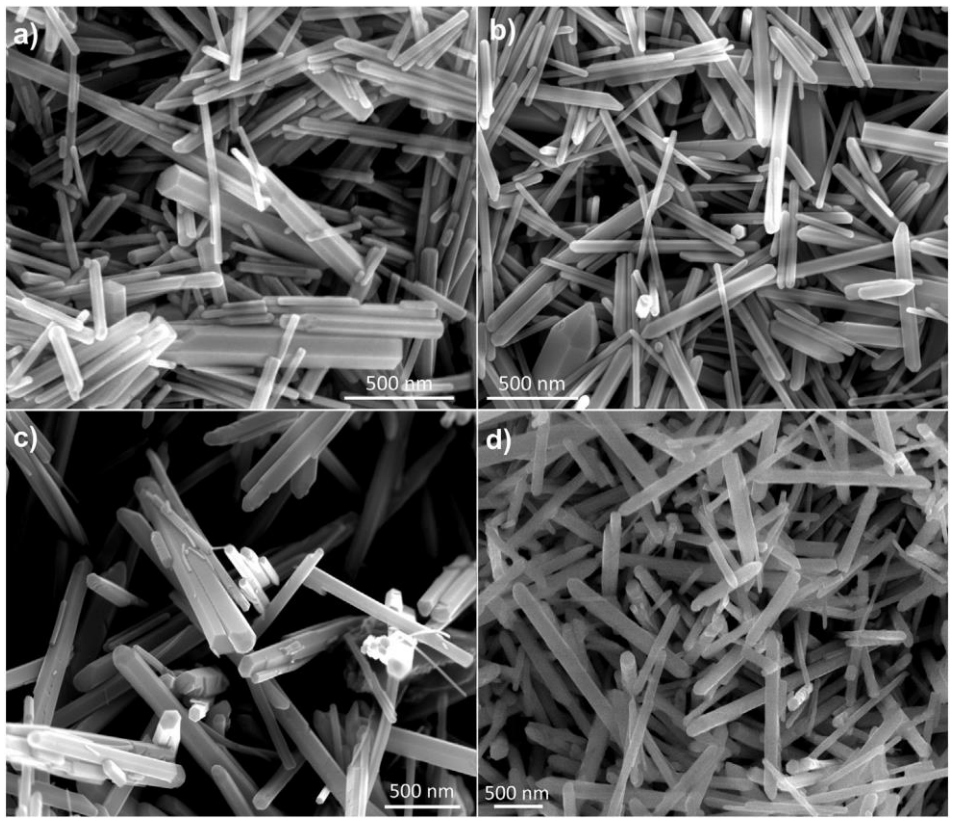

Figure 18. HR-SEM images of ZnO NWs with 0% (a), 5% (b), 7.5%(c), and 15%(d) of Co.

TEM images of pure (Figure 19a,-c) and 5% Co-doped (Fig. Figure 19b,-c) ZnO NWs confirmed the observations made in HR-SEM. Growth direction was revealed by measuring the interplanar distance for both set of samples. Interplanar distance was about 2.8 Å which corresponds to the [01–10] planes of hexagonal ZnO. [01–10] planes are perpendicular to the [0001] planes indicating that both set of samples had hexagonal wurtzite structure with growth direction of [0001]. In addition, TEM images revealed a highly crystalline structure for both sets of samples (Figure 19c-d). This confirms that the Co atoms were uniformly incorporated into the ZnO lattice.

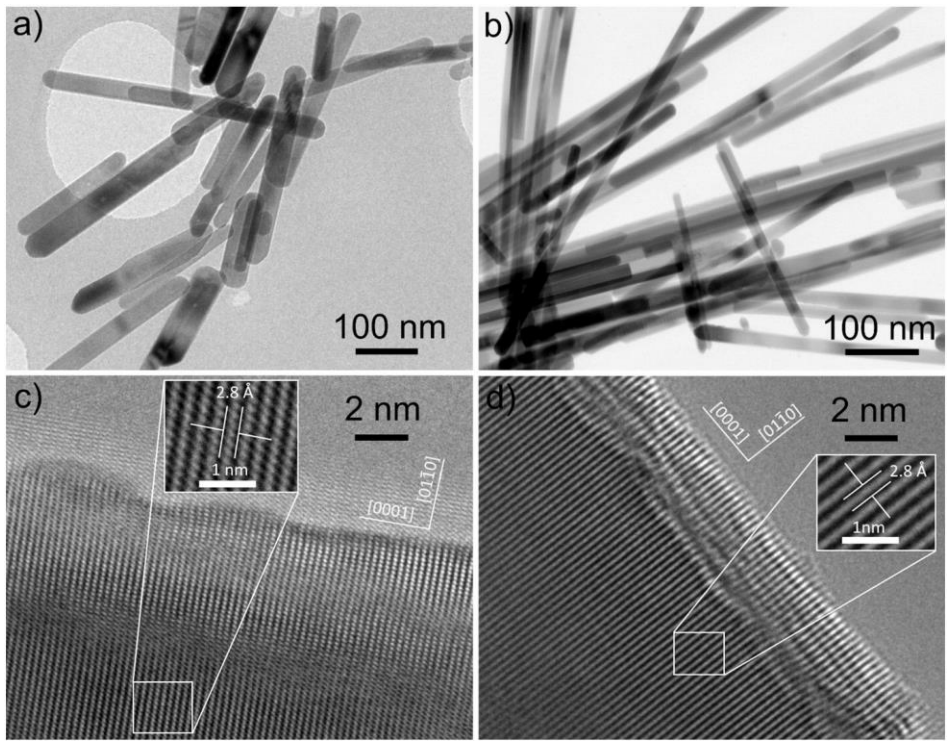

Figure 19. TEM images of pure (a,c) and 5% Co-doped ZnO NWs (b,d).

4.3.3. Mechanical properties of ZnO and Co-doped ZnO nanowires

Mechanical characterization was conducted by comparing the Young's modulus and bending strength values of pure and 5% Co-doped ZnO NWs. 5% Co-doped ZnO NWs was chosen due to the inhomogeneous morphology and presents of structural defects at higher concentrations of doping which would lead to numerous errors in determination of mechanical properties. Young's modulus

was determined using three-point bending configuration inside AFM described in section 3.2.2. Altogether 22 pure and 25 Co-doped ZnO NWs with diameters between 20–59 nm and 21–151 nm were measured. Young's modulus values vs diameter for pure and 5% Co-doped ZnO NWs are plotted on Figure 20. The diameter dependent behavior of the Young's modulus was evident for pure ZnO NWs below 40 nm. For larger diameters, the average value was approximately 120 GPa which is slightly lower than for bulk ZnO (144 GPa). The obtained results are close to several previously measured values of Young's modulus values of ZnO NWs [38,40,54].

Comparing the Young's modulus values of pure and 5% Co-doped ZnO NWs with similar diameters (between 20 to 40 nm) revealed that doping reduced the value by about a third. This result is contradictory to previous study, where it was found that doping with Indium (In) lead to an increase in Young's modulus values of ZnO NWs [109]. Possible explanation to the difference in observed effect on mechanical properties include difference in doping material, synthesis process and growth direction. In cation is larger than Zn cation and therefore increases the volume of the unit cell and induces additional stresses. Synthesis process was varied to produce In-doped ZnO NWs as opposed to our case, where no changes were made. In addition, In-doped ZnO NWs exhibited a different growth direction compared to pure ZnO NWs, [-1010] and [0001], respectively. Finally, the reported Young's modulus values of pure ZnO NWs were much lower (58GPa) than in most of the reliable studies on ZnO NWs which may indicate low quality of the NWs. Decrease of Young's modulus due to Co doping can be explained by the increase of point defects. Isovalent doping of Co is expected to cause single point defects. Previous experimental [40] and theoretical [76,77] studies have demonstrated that increased concentration of point defects can affect the mechanical properties of NWs including the decrease of Young's modulus values.

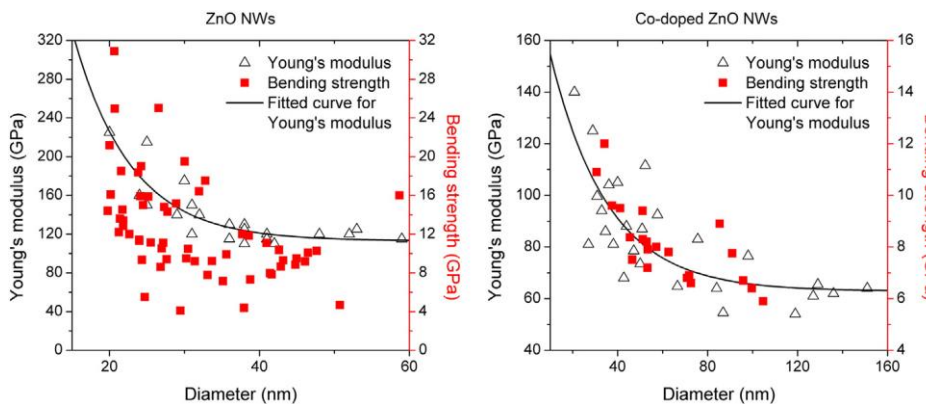

Figure 20. Young's modulus and bending strength values of pure (left) and 5% Co-doped (right) ZnO NWs.

Bending strength tests were performed inside HR-SEM using cantilever beam bending test described in section 3.2.1.2. Calculation of bending strength requires the knowledge of exact Young's modulus value of the tested material. Therefore, polynomial curve was fitted to the experimentally measured Young's modulus values due to their diameter dependent nature. The equation of the fitted curve was used to find the Young's modulus value for each NW diameter used in the bending strength measurement. In total 59 pure ZnO NWs with diameters ranging from 20 to 61 nm and 21 Co-doped NWs with diameter between 31 and 105 were measured. Again, clear sized dependence was revealed with the effect becoming prominent below 40 nm and 80 nm for pure and Co-doped ZnO NWs, respectively (Figure 20). The bending strength values for pure ZnO NWs with the diameter higher than 40 nm were close to previously reported values of 7.7 GPa [39] and 7 GPa [110]. Diameter dependence of bending strength values was due to the change in the point defect concentration [75]. The measured values in this study for both set of samples were closed to the theoretical strength which is known to be approximately Young's modulus value divided by ten based on the atomic bonding consideration [111]. Therefore, NWs were of high quality with low concentration of major structural defects and addition of moderate concentrations of Co did not introduce addition critical defects.

4.4. Effect of Al_2O_3 coating on the mechanical properties of Au and Ag nanowires (publication IV)

In this section, effect of oxide coating on the mechanical properties of one-dimensional nanostructures was studied. Silver (Ag) and gold (Au) nanowires were chosen as core material due to their unique structure, well-known properties and wide range of potential application. Properties of these NWs can be efficiently modified by coating them with a thin layer of oxide coating, resulting in novel metal-oxide core-shell NWs [112,113]. Theoretical studies of core-shell nanostructures have predicted number of interesting effects, for example the core-shell interface may significantly influence the overall plastic response or lead to non-linear dependence of Young's modulus on the composition of the core-shell NWs [81,82]. In the current study, atomic layer deposition (ALD) was used to coat the metallic NWs with thin layer of Al_2O_3. ALD allowed for precise deposition with uniform coating thickness. Core-shell NWs were characterized using HR-SEM and TEM and the mechanical properties were measured using AFM- and SEM-based nanomanipulation methods.

4.4.1. Preparation of core-shell nanowires

Commercially available metallic NWs were used in the present study. Ag NWs were purchased form *Blue Nano* (USA) and Au NWs from *Smart Materials* (Latvia). NWs were deposited from solution onto two types of substrates: TEM grids for cantilever beam bending inside HR-SEM and silicon substrate with inverted pyramids for AFM-based bending experiments. All samples were heated to 200°C for 5 min to remove possible solvent and surfactant residues. Next, samples were placed inside a home-built ALD reactor for low-temperature coating with Al_2O_3. Coating of metallic NWs was carried out at 150°C by applying 100 cycles of $Al(CH_3)_3$ and H_2O as precursors. Precursors were kept at room temperature and carried into the reaction zone separately by dry inert gas (N_2). Each deposition cycle consisted of 3 s metal precursor supply followed by 2 s inert gas purge, 5 s oxygen precursor supply and 5 s purge. During coating process gas pressure ranged from 230–240 Pa in the reaction zone.

4.4.2. Structural characterization of core-shell nanowires

Structural characterization of individual uncoated and alumina coated metallic NWs was performed by Helios HR-SEM and TEM. Uncoated Ag and Au NWs were straight and uniform with a well-pronounced pentagonal cross-section and diameters ranging from tens to several hundred nanometers. The NWs preserved their pentagonal geometry and quality during the coating process. The HR-SEM and TEM images demonstrated that the coating was relatively smooth and uniform (Figure 21a,-b) and with an amorphous structure (Figure 21c). The alumina shell gave a good electron contrast to the Ag and Au core, enabling reliable estimation of the coating thickness from the images. In addition, AFM images of several Ag and Au NWs before and after coating were taken to obtain additional information about the coating thickness. The methods were consistent with each other and coating thickness value of approximately 16 nm was determined.

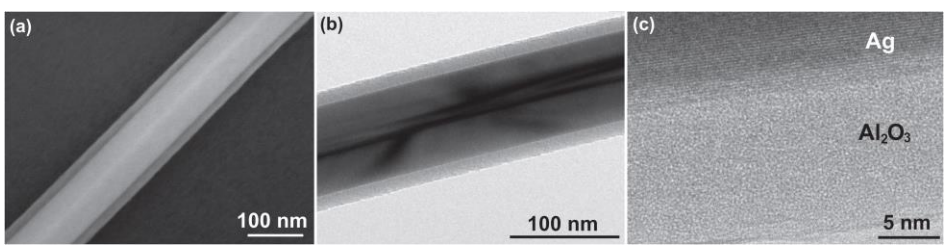

Figure 21. HR-SEM image of Au/Al_2O_3 NWs (a) and TEM images of Ag/Al_2O_3 NWs (b-c).

4.4.3. Mechanical characterization of core-shell nanowires

Measurement of Young's modulus and bending strength values of uncoated and alumina coated Au NWs was performed using AFM-based three-point bending and cantilever beam bending methods described in section 3.2.2. Au NWs were chosen because of the similar mechanical and structural properties between Ag and Au and since the mechanical properties of pentagonal Au NWs have not been previously investigated. The results of the measurements revealed a noticeable increase in Young's modulus of the core-shell NWs due to the alumina coating. Young's modulus values as a function of diameter for uncoated and coated Au NWs can be seen in Figure 21a. Comparing the two curves shows that on average NWs with alumina coating have 30–50 GPa higher Young's modulus values. Also, it was noticed that the values increase as the diameter is decreased. In case of core-shell NWs, this dependence is due to the increase contribution of the stiffer coating with constant thickness in addition to the general size effect. The approximate Young's modulus value of the alumina coating was deduced through simple mathematical consideration using the average Young's modulus values of core-shell and uncoated Au NWs. The calculated Young's modulus of alumina coating was 160±30 GPa which is consistent with literature data (150–182 GPa) for similarly produced amorphous ALD alumina coatings [114]. In addition, AFM force curves and SEM images of the broken NWs revealed a brittle nature for the alumina coating (Figure 23).

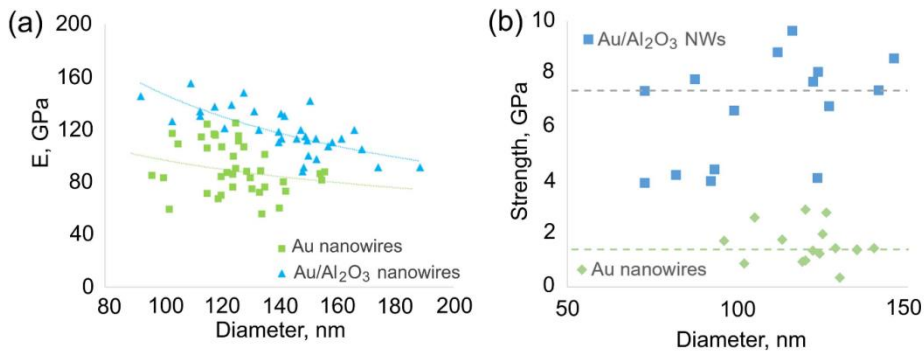

Figure 22. Young's modulus (a) and bending strength (b) values of pure Au and Au/Al_2O_3 NWs.

In contrast to Young's modulus values, the difference in strength between the coated and the uncoated NWs was much higher (Figure 21b). Median yield strength of alumina coated and uncoated Au NWs were 7.4 and 1.4 GPa, respectively. In addition, it was observed that the coating had a protective effect on the core material, allowing the Au NWs to tolerate higher degrees of deformation. A possible explanation of the increased fracture resistance of the core was that the

alumina shell confined the metal core of the NW and might have prevented the nucleation of defects at the core-shell interface and intrinsic structural transformation, such as kinking or twinning observed during deformation [115]. Alternatively, creation of dislocation networks at the core/shell interface may act as sources for formation of new dislocations [116]. When dislocation sources in the coating are operational, dislocation pile-ups occur at the interface, exerting back stress upon the dislocation source. The back stress from the dislocation pile-ups leads to an elevated flow stress making the metal core stronger.

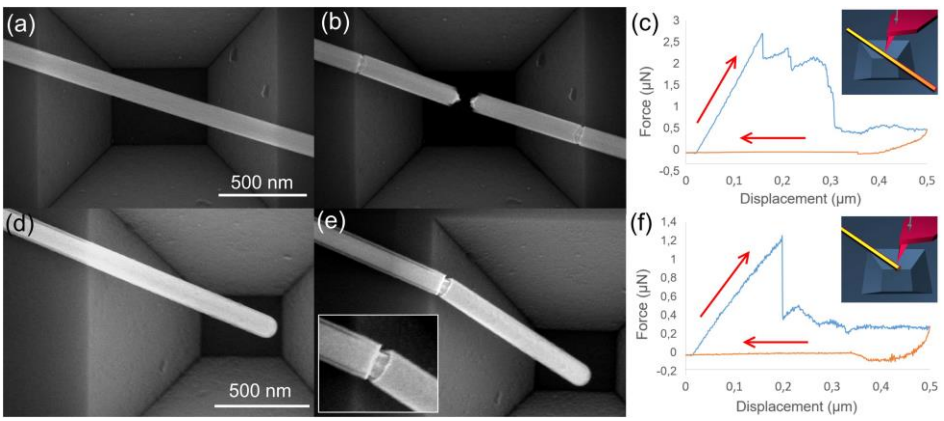

Figure 23. Alumina coated Au NWs before (a,d) and after (b,e) bending test inside AFM and corresponding force-displacement curves (c,f).

Suspended NWs in cantilever configuration were bent inside HR-SEM to investigate the influence of the electron beam (EB) on the response of the NWs to bending deformation. Uncoated Ag and Au NWs behaved purely elastically until plastic deformation occurred, irrespective of the presence of the EB. Alumina coated NWs slowly (over several minutes) restored their initial straight profiles when they were bent close to the plastic yield point of the core under EB radiation. The restoration dynamics composed of two regimes: fast linear followed by exponential decay. If the EM was switched off during the restoration stage, shape restoration ceased, and the NW profile was "frozen" at the given curvature. A soon as the beam was switched on again, shape restoration resumed. In addition, shape restoration effect was strongly dependent on deformation rate. Rapidly deformed core-shell NWs exhibited purely elastic behavior regardless of EB state and parameters. At lower deformation rates or provided that the NWs were kept in a bent state for several seconds, slow shape restoration was observed. When NWs were bent beyond the yield point of the core, initial straight profile was not achieved. In total, 17 Ag/Al_2O_3 and five Au/Al_2O_3 were bent and shape restoration was observed for all of them even when bent multiple times.

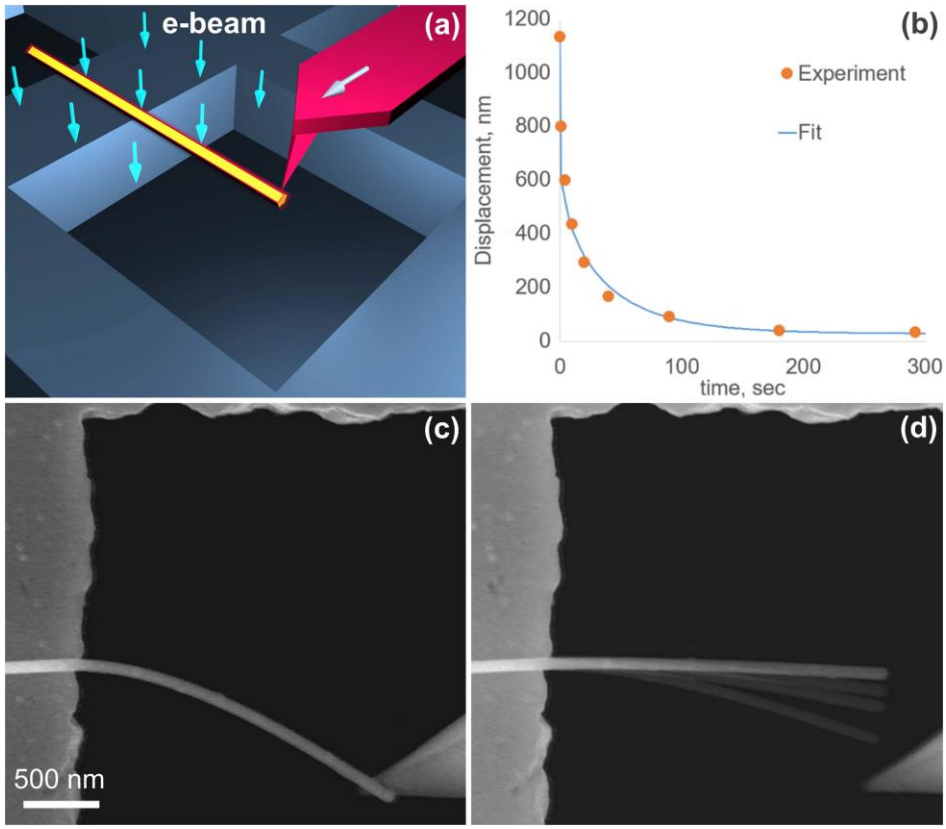

Figure 24. Cantilever beam bending scheme under EB radiation (a). Bent Ag/Al_2O_3 NW was held for 30 s (a) and when released a slow restoration of the initial profile took place (d). Corresponding restoration dynamic (b).

The influence of EB parameters on NW behavior was evaluated by bending the same core-shell NW at different EB voltages, probe currents, scan rates, and magnifications. It was found both EB voltage and scan rate had no significant effect on the restoration dynamics. From this we can conclude that at all of the voltages used (5–15 kV) the electrons had sufficient energy to induce changes in the material. The impact of the current and magnification was considerable. At higher currents, the restoration was faster which can be explained by the higher number of electrons passing through the shell per time unit. Similarly, higher magnification means that NW occupies a larger fraction of the SEM images and therefore is exposed to higher number of electrons per on image resulting in faster restoration.

Based on the results, shape restoration process can be understood as EB induced structural relaxation of the shell followed by elastic core driven restoration. EB has enough energy to break Al-O bond, create oxygen vacancies and subsequently cause the rearrangement of atoms in the amorphous shell [65].

This means that the shell undergoes transition from an elastic to a stress-free plastic deformation during the bending process. When the external force is removed, new equilibrium state is determined by the interplay between restoring elastically bent core and resting relaxed shell. This is followed by a slow EB-driven restoration process, where again stresses created in the shell are relaxed by rearrangement of atoms. Closer to the initial straight profile, the less energy remains in the deformed core the smaller the amount of restoration.

This kind of dynamics of shape restoration resemble the behavior of visco-elastic material. Therefore, the overall response of the core-shell system can be alternatively described as an interplay between the elasticity of core and the EB-induced viscosity of the shell. Term viscosity in this case is abstract, as the phenomenon is more complexed, but allows for quantitative description of the process. Finite element method (FEM) was used to calculate effective viscosity of the shell using real experimental values. FEM simulation resulted in viscosity values between 10^{11}–10^{13} Pa·s, depending on EB current and magnification.

5. SUMMARY

In the present thesis, detailed structural and mechanical characterization of one-dimensional metal-oxide nanostructures (1D MONS) was carried out. The main goal was to determine the underlying relationship between the mechanical and structural properties. In order to achieve this goal, different factors which affect the structure of 1D MONS were systematically studied. Structural characterization was carried out by electron microscopy, X-ray diffraction (XRD) and Raman spectroscopy. Two different bending tests were used for mechanical characterization – cantilever beam bending and three-point bending. The mechanical characterization was carried out either by nanomanipulation setups inside scanning electron microscope (SEM) or atomic force microscope (AFM). The main activities and result were as follows.

TiO_2 nanofibers were produced using the same precursor but different electrospinning technique to see how slight difference in synthesis process can affect the structural and mechanical properties of 1D MONS. Structural characterization revealed similar polycrystalline structure for needle and needless electrospinning. For the first time, comparative study of the mechanical properties of TiO_2 nanofibers produced by different techniques was carried out using cantilever beam bending inside SEM. Both Young's modulus and bending strength measurements yielded very similar results for the two techniques. However, Weibull analysis suggested that TiO_2 nanofibers produced by needle electrospinning were more uniform in microstructure and mechanical behavior.

The effect of annealing on 1D MONS was determined by comparing the structural and mechanical properties of Al_2O_3 nanofibers before and after heating at 1400°C for 1 h. The structural characterization revealed a phase transition from polycrystalline γ-Al_2O_3 to monocrystalline α-Al_2O_3 due to the annealing. Mechanical properties before and after annealing Al_2O_3 nanofibers were measured using cantilever beam bending method inside SEM. Compared to previous results, more reliable Young's modulus values were obtained for Al_2O_3 nanofibers. Phase transition of Al_2O_3 nanofibers increased the Young's modulus and bending strength values. Novel branched structure with superior mechanical properties was observed for annealed samples due to fusion of intersecting nanofibers.

The role of defects on the structural and mechanical properties of 1D MONS was determined by comparing pure ZnO nanowires to Co-doped ZnO nanowires. In order to eliminate influence of synthesis process, the nanowires were produced using the same synthesis method and the doped samples were obtained only by changing the precursor content. Structural characterization revealed that up to 20% Co could be incorporated into ZnO crystal structure without phase separation and minimal effect on the crystal lattice. At the same time, change in nanowire morphology was observed for samples starting from 7.5% Co content. For the first time, comparative mechanical characterization of pure and doped 1D MONS produced by similar growth conditions was carried

out using AFM- and SEM-based bending methods. Measurements revealed that doping by Co decreased the mechanical properties of ZnO nanowires due to increase of point defects.

Effect of oxide coating on 1D NS was determined by studying the mechanical properties of Al_2O_3 coated Au and Ag nanowires. Atomic layer deposition was used to coat the metallic nanowires and the mechanical characterization was carried out by AFM- and SEM-based nanomanipulation experiments. Electron microscopy revealed that the alumina coating was smooth and uniform and with an amorphous structure. Mechanical characterization using AFM showed that the coating protected the core material from fracture and plastic yield, allowing it to withstand higher deformations and stresses compared to uncoated nanowires. In addition, bend tests inside SEM revealed that electron beam can induce reversible elastic-to-plastic transition in Ag/Al_2O_3 and Au/Al_2O_3 nanowires.

The results of the present thesis show how intertwined the mechanical and structural properties of 1D MONS are and which different factors related to structure can influence the mechanical response. In the present study, only some of the key factors and materials have been discussed. Further studies are required in order to obtain 1D MONS with predictable properties and thereby expand the applicability.

6. SUMMARY IN ESTONIAN

Ühedimensionaalsete metalloksiid nanostruktuuride struktuuritundlikud mehaanilised omadused

Käesolevas doktoritöös uuriti erinevaid ühedimensionaalseid metalloksiid nanostruktuure (1D MONS-e). Töö peamiseks eesmärgiks oli leida seos nende struktuuri eripärade ja mehaaniliste omaduste vahel. Selleks uuriti süstemaatiliselt erinevaid 1D MONS-ide struktuuri mõjutavaid tegureid – valmistamismeetod, kuumutamine, defektid ja oksiidikihiga katmine. Struktuuri uurimiseks kasutati elektronmikroskoopiat, röntgendifraktsiooni (XRD-i) ja Raman spektroskoopiat. Mehaaniliste omaduste mõõtmiseks rakendati kahte erinevat paindekatset – konsooltala ja kolme punkti paindekatset. Katsed teostati nanomanipulatsiooni süsteemi abil skaneerivas elektronmikroskoopis (SEM-is) või aatomjõumikroskoobis (AFM-is). Töö peamised tulemused olid järgnevad.

Leidmaks, millist mõju avaldab 1D MONS-i sünteesiprotsessi muutmine nende struktuurile ja mehaanilistele omadustele, valmistati TiO_2 nanofiibrid kasutades sama lähteainet aga kahte erinevat elektroketramise meetodit – nõelaga ja nõelata. Võrreldes kahe meetodi abil valmistatud nanofiibrite struktuuri leiti, et mõlemal on sarnane polükristallne struktuur. Kasutades konsooltala paindekatset SEM-is, teostati esmakordselt võrdlev mehaaniliste omaduste mõõtmine kahel erineval moel valmistatud TiO_2 nanofiibritega. Mõõtmiste tulemusena leiti, et erineval moel valmistatud nanofiibrite Youngi mooduli ja paindetugevuse väärtused olid väga sarnased. Samal ajal näitas aga Weibulli statistika, et nõelaga valmistatud TiO_2 nanofiibrid mikrostruktuur ja mehaanilised omadused olid ühtlasemad.

Selleks, et uurida kuumutamise mõju 1D MONS-i struktuurile ja mehaanilistele omadustele, võrreldi Al_2O_3 nanofiibreid enne ja pärast kuumutamist 1400°C-il. Leiti, et kuumutamisel toimub nanofiibrites faasisiire polükristallilisest γ-Al_2O_3 monokristalliliseks α-Al_2O_3. Sarnaselt TiO_2 kasutati ka siinkohal mehaaniliste omaduste määramiseks konsooltala paindekatset SEM-is. Mõõtmiste tulemusena leiti, et faasisiire suurendab Al_2O_3 nanofiibrite Youngi moodulit ja paindetugevust. Lisaks moodustus kuumutamise käigus nanofiibritest uudne parenenud mehaaniliste omadustega kärgstruktuur.

Defektide mõju uurimiseks võrreldi ZnO nanotraatide mehaanilisi ja struktuurseid omadusi koobaltiga (Co) dopeeritud ZnO nanotraatidega. Välistamaks sünteesiprotsessi mõju, valmistati mõlemat tüüpi nanotraadid sama meetodi abil. Dopeeritud nanotraatide valmistamiseks muudeti vaid lähteainete koostist. Uurides dopeeritud nanotraatide struktuuri leiti, et kuni 20% ZnO on võimalik Co asendada ilma, et toimuks faasieraldust ning märkimisväärset muutust ZnO kristallstruktuuris. Autori teada on tegu esmakordse samal sünteesimeetodil valmistatud dopeerimata ja dopeeritud 1D MONS mehaaniliste omaduste võrdlemisega. Mõõtmisteks kasutati nii konsooltala kui ka kolme punkti paindekatseid, mis viidi läbi AFM-is ja SEM-is. Katsete tulemusel leiti, et Co

dopeerimine vähendab ZnO Youngi mooduli ja paindetugevuse väärtusi punkt-defektide kontsentratsiooni suurenemise tõttu.

Leidmaks, millist mõju omab oksiidikate ühedimensionaalsele nano-struktuurile, uuriti Al_2O_3 kaetud Au ja Ag nanotraatide mehaanilisi omadusi. Metallnanotraatide katmiseks kasutati aatomkihtsadestamist ning mehaanilisi omadusi mõõdeti taaskord AFM-is ja SEM-is. Elektronmikroskoobi piltidelt leiti, et Al_2O_3 kiht oli ühtlane ja amorfse struktuuriga. Mõõtes AFM-iga mehaanilisi omadusi näidati, et oksiidne kate (kest) kaitses kaetud materjali (tuuma) purunemise eest ja suurendas kõvadust, mistõttu talusid vastavad tuum-kest struktuurid suuremat deformatsiooni ja pinget võrreldes katmata nanotraatidega. Lisaks leiti SEM-is tehtud paindekatsete käigus, et elektronkiir põhjustab tuum-kest nanotraatides pööratavat üleminekut elastsest deformatsioonist plastseks deformatsiooniks.

Käesoleva doktoritöö tulemused näitavad, kuivõrd seotud on 1D MONS-ide mehaanilised ja struktuursed omadused ning millised struktuuriga seotud asjaolud võivad mõjutada materjali mehaanilisi omadusi. Antud töö käigus jõuti uurida vaid mõnda levinud materjali ja neid mõjutavaid võtmetegureid. Autori hinnangul vajab antud valdkond pikemat süvitsi uurimist. Edasine teadustöö on vajalik, et valmistada sihipäraste kindlate mehaaniliste ja struktuursete omadustega ühedimensionaalseid metalloksiid nanostruktuure, seeläbi võimaldades neid kasutada erinevates rakendustes.

ACKNOWLEDGMENTS

First of all, I would like to thank my supervisors Sergei Vlassov and Ergo Nõmmiste for their comprehensive support and guidance throughout my PhD studies. I am also very grateful to all of my colleague at the Laboratory of Physics of Nanostructures and nanomanipulation workgroup. Special thanks to Mikk Antsov and Sven Oras for all of the help and moral support to get though PhD studies. I would also like to thank my co-authors for a pleasant and fruitful cooperation, especially Andris Šutka for synthesis of nanofibers and nanowires and Boris Polyakov for TEM measurements and help on preparing the manuscripts. Finally, I would like to thank my family, friends and especially dear life partner Maarja for all of their support throughout my studies.

This work was supported by Estonian Research Council grants IUT2-25, PUT1689, ETF9007; Center of Excellence TK114 and COST Actions MP1303. This work has been partially supported by Graduate School of Functional materials and technologies receiving funding from the European Regional Development Fund in University of Tartu, Estonia.

REFERENCES

[1] Pokropivny V. V. and Skorokhod V. V. (2007) Classification of nanostructures by dimensionality and concept of surface forms engineering in nanomaterial science. *Mater. Sci. Eng. C* 27 990–3

[2] Devan R. S., Patil R. A., Lin J.-H. and Ma Y.-R. (2012) One-Dimensional Metal-Oxide Nanostructures: Recent Developments in Synthesis, Characterization, and Applications. *Adv. Funct. Mater.* 22 3326–70

[3] Bhushan B. (2010) *Springer Handbook of Nanotechnology*. Berlin, Springer

[4] Emeline A. V., Kataeva G. V., Panasuk A. V., Ryabchuk V. K., Sheremetyeva N. V. and Serpone N. (2005) Effect of Surface Photoreactions on the Photocoloration of a Wide Band Gap Metal Oxide: Probing Whether Surface Reactions Are Photocatalytic. *J. Phys. Chem. B* 109 5175–85

[5] Gutowski M., Jaffe J. E., Liu C.-L., Stoker M., Hegde R. I., Rai R. S. and Tobin P. J. (2002) Thermodynamic stability of high-K dielectric metal oxides ZrO2 and HfO2 in contact with Si and SiO2. *Appl. Phys. Lett.* 80 1897

[6] Sysoev V. V., Button B. K., Wepsiec K., Dmitriev S. and Kolmakov A. (2006) Toward the Nanoscopic "Electronic Nose": Hydrogen vs Carbon Monoxide Discrimination with an Array of Individual Metal Oxide Nano- and Mesowire Sensors. *Nano Lett.* 6 1584–8

[7] Lee M.-J., Han S., Jeon S. H., Park B. H., Kang B. S., Ahn S.-E., Kim K. H., Lee C. B., Kim C. J., Yoo I.-K., Seo D. H., Li X.-S., Park J.-B., Lee J.-H. and Park Y. (2009) Electrical Manipulation of Nanofilaments in Transition-Metal Oxides for Resistance-Based Memory. *Nano Lett.* 9 1476–81

[8] Takada K., Sakurai H., Takayama-Muromachi E., Izumi F., Dilanian R. A. and Sasaki T. (2003) Superconductivity in two-dimensional CoO_2 layers. *Nature* 422 53

[9] Kumar M. A., Jung S. and Ji T. (2011) Protein Biosensors Based on Polymer Nanowires, Carbon Nanotubes and Zinc Oxide Nanorods. *Sensors* 11 5087–111

[10] Moon J., Park J.-A., Lee S.-J., Zyung T. and Kim I.-D. (2010) Pd-doped TiO2 nanofiber networks for gas sensor applications. *Sens. Actuators B Chem.* 149 301–5

[11] Rosario R., Gust D., Garcia A. A., Hayes M., Taraci J. L., Clement T., Dailey J. W. and Picraux S. T. (2004) Lotus Effect Amplifies Light-Induced Contact Angle Switching. *J. Phys. Chem. B* 108 12640–2

[12] Song M. Y., Kim D. K., Ihn K. J., Jo S. M. and Kim D. Y. (2004) Electrospun TiO2 electrodes for dye-sensitized solar cells. *Nanotechnology* 15 1861

[13] Chuangchote S., Jitputti J., Sagawa T. and Yoshikawa S. (2009) Photocatalytic Activity for Hydrogen Evolution of Electrospun TiO2 Nanofibers. *ACS Appl. Mater. Interfaces* 1 1140–3

[14] Prades J. D., Jimenez-Diaz R., Hernandez-Ramirez F., Fernandez-Romero L., Andreu T., Cirera A., Romano-Rodriguez A., Cornet A., Morante J. R., Barth S. and Mathur S. (2008) Toward a Systematic Understanding of Photodetectors Based on Individual Metal Oxide Nanowires- *J. Phys. Chem. C* 112 14639–44

[15] Kim J., Yun J.-H., Kim C. H., Park Y. C., Woo J. Y., Park J., Lee J.-H., Yi J. and Han C.-S. (2010) ZnO nanowire-embedded Schottky diode for effective UV detection by the barrier reduction. effect *Nanotechnology* 21 115205

[16] Nguyen P., Ng H. T., Yamada T., Smith M. K., Li J., Han J. and Meyyappan M. (2004) Direct Integration of Metal Oxide Nanowire in Vertical Field-Effect Transistor. *Nano Lett.* 4 651–7
[17] Li C., Fang G., Xu S., Zhao D. and Zhao X. (2006) Phase-segregation assisted growth of quasi-aligned ZnO nanorods on a Mg0.6Zn0.4O-coated Si substrate by thermal evaporation. *Nanotechnology* 17 5367
[18] Huczko A. (2000) Template-based synthesis of nanomaterials. *Appl. Phys. A* 70 365–76
[19] Yan X.-M., Kwon S., Contreras A. M., Bokor J. and Somorjai G. A. (2005) Fabrication of Large Number Density Platinum Nanowire Arrays by Size Reduction Lithography and Nanoimprint Lithography. *Nano Lett.* 5 745–8
[20] Boyd D. A., Greengard L., Brongersma M., El-Naggar M. Y. and Goodwin D. G. (2006) Plasmon-Assisted Chemical Vapor Deposition. *Nano Lett.* 6 2592–7
[21] Limmer S. J. and Cao G. (2003) Sol–Gel Electrophoretic Deposition for the Growth of Oxide Nanorods. *Adv. Mater.* 15 427–31
[22] Su J., Feng X., Sloppy J. D., Guo L. and Grimes C. A. (2011) Vertically Aligned WO3 Nanowire Arrays Grown Directly on Transparent Conducting Oxide Coated Glass: Synthesis and Photoelectrochemical Properties. *Nano Lett.* 11 203–8
[23] Zhou J., Fei P., Gao Y., Gu Y., Liu J., Bao G. and Wang Z. L. (2008) Mechanical−Electrical Triggers and Sensors Using Piezoelectric Micowires/ Nanowires. *Nano Lett.* 8 2725–30
[24] Yuan Q., Zhao Y.-P., Li L. and Wang T. (2009) Ab Initio Study of ZnO-Based Gas-Sensing Mechanisms: Surface Reconstruction and Charge Transfer. *J. Phys. Chem. C* 113 6107–13
[25] Wang Z. L. (2004) Zinc oxide nanostructures: growth, properties and applications. *J. Phys. Condens. Matter* 16 R829
[26] Cui J. (2012) Zinc oxide nanowires *Mater. Charact.* 64 43–52
[27] Ge M., Cao C., Huang J., Li S., Chen Z., Zhang K.-Q., Al-Deyab S. S. and Lai Y. (2016) A review of one-dimensional TiO2 nanostructured materials for environmental and energy applications. *J. Mater. Chem. A* 4 6772–801
[28] Hudson L. K., Misra C., Perrotta A. J., Wefers K. and Williams F. S. (2000) Aluminum Oxide. *Ullmann's Encyclopedia of Industrial Chemistry*. Wiley-VCH Verlag GmbH & Co
[29] Peng X. S., Zhang L. D., Meng G. W., Wang X. F., Wang Y. W., Wang C. Z. and Wu G. S. (2002) Photoluminescence and Infrared Properties of α-Al2O3 Nanowires and Nanobelts. *J. Phys. Chem. B* 106 11163–7
[30] Kim J.-H., Yoo S.-J., Kwak D.-H., Jung H.-J., Kim T.-Y., Park K.-H. and Lee J.-W. (2014) Characterization and application of electrospun alumina nanofibers. *Nanoscale Res. Lett.* 9 44
[31] Ramesh K. T. (2009) *Nanomaterials – Mechanics and Mechanisms*. Boston, Springer US
[32] Zhai T., Fang X., Liao M., Xu X., Zeng H., Yoshio B. and Golberg D. (2009) A Comprehensive Review of One-Dimensional Metal-Oxide Nanostructure Photodetectors. *Sensors* 9 6504–29
[33] Zhang Q., Wang H.-Y., Jia X., Liu B. and Yang Y. (2013) One-dimensional metal oxide nanostructures for heterogeneous catalysis. *Nanoscale* 5 7175
[34] Li Y., Yang X.-Y., Feng Y., Yuan Z.-Y. and Su B.-L. (2012) One-Dimensional Metal Oxide Nanotubes, Nanowires, Nanoribbons, and Nanorods: Synthesis,

Characterizations, Properties and Applications. *Crit. Rev. Solid State Mater. Sci.* 37 1–74
[35] Sharma R., Bisen D. P., Shukla U. and Sharma B. G. (2012) X-ray diffraction: a powerful method of characterizing nanomaterials. *Recent Res. Sci. Technol.* 4 77–79
[36] Agrawal R., Peng B., Gdoutos E. E. and Espinosa H. D. (2008) Elasticity Size Effects in ZnO Nanowires − A Combined Experimental-Computational Approach. *Nano Lett.* 8 3668–74
[37] Desai A. V. and Haque M. A. (2007) Mechanical properties of ZnO nanowires. *Sens. Actuators Phys.* 134 169–76
[38] He M.-R., Shi Y., Zhou W., Chen J. W., Yan Y. J. and Zhu J. (2009) Diameter dependence of modulus in zinc oxide nanowires and the effect of loading mode: *In situ* experiments and universal core-shell approach. *Appl. Phys. Lett.* 95 091912
[39] Hoffmann S., Östlund F., Michler J., Fan H. J., Zacharias M., Christiansen S. H. and Ballif C. (2007) Fracture strength and Young's modulus of ZnO nanowires. *Nanotechnology* 18 205503
[40] Wang X., Chen K., Zhang Y., Wan J., Warren O. L., Oh J., Li J., Ma E. and Shan Z. (2015) Growth Conditions Control the Elastic and Electrical Properties of ZnO Nanowires. *Nano Lett.* 15 7886–92
[41] Xu F., Qin Q., Mishra A., Gu Y. and Zhu Y. (2010) Mechanical properties of ZnO nanowires under different loading modes. *Nano Res.* 3 271–80
[42] Zhang Y., Ru C., Liu X., Zhong Y., Sun X., Hoyle D., Cotton I. and Sun Y (2010) A MEMS tensile testing device for mechanical characterization of individual nanowires. *IEEE* 2581–4
[43] Manoharan M. P., Desai A. V., Neely G. and Haque M. A. (2008) Synthesis and Elastic Characterization of Zinc Oxide Nanowires. *J. Nanomater.* 2008 1–7
[44] Polyakov B., Dorogin L. M., Vlassov S., Kink I., Lohmus A., Romanov A. E. and Lohmus R. (2011) Real-time measurements of sliding friction and elastic properties of ZnO nanowires inside a scanning electron microscope. *Solid State Commun.* 151 1244–7
[45] Song J., Wang X., Riedo E. and Wang Z. L. (2005) Elastic Property of Vertically Aligned Nanowires. *Nano Lett.* 5 1954–8
[46] Bo A., Zhan H., Bell J., Zhu H. and Gu Y. (2014) Mechanical bending properties of sodium titanate ($Na_2Ti_3O_7$) nanowires. *RSC Adv* 4 56970–6
[47] Ni H., Li X. and Gao H. (2006) Elastic modulus of amorphous SiO2 nanowires. *Appl. Phys. Lett.* 88 043108
[48] Tan E. P. S., Zhu Y., Yu T., Dai L., Sow C. H., Tan V. B. C. and Lim C. T. (2007) Crystallinity and surface effects on Young's modulus of CuO nanowires. *Appl. Phys. Lett.* 90 163112
[49] Wen B., Sader J. E. and Boland J. J. (2008) Mechanical Properties of ZnO Nanowires. *Phys. Rev. Lett.* 101 175502
[50] Stan G., Ciobanu C. V., Parthangal P. M. and Cook R. F. (2007) Diameter-Dependent Radial and Tangential Elastic Moduli of ZnO Nanowires. *Nano Lett.* 7 3691–7
[51] Fang T.-H. and Chang W.-J. (2004) Nanolithography and nanoindentation of tantalum-oxide nanowires and nanodots using scanning probe microscopy. *Phys. B Condens. Matter* 352 190–9
[52] Jiang D., Tian C., Liu Q., Zhao M., Qin J., Hou J., Gao S., Liang Q. and Zhao J. (2014) Young′s modulus of individual ZnO nanowires. *Mater. Sci. Eng. A* 610 1–4

[53] Gladwell G. M. L. (1980) *Contact problems in the classical theory of elasticity*. Alphen aan den Rijn, The Netherlands, Sijthoff & Noordhoff
[54] Chen C. Q., Shi Y., Zhang Y. S., Zhu J. and Yan Y. J. (2006) Size Dependence of Young's Modulus in ZnO Nanowires. *Phys. Rev. Lett.* 96 075505
[55] Huang Y., Bai X. and Zhang Y. (2006) In situ mechanical properties of individual ZnO nanowires and the mass measurement of nanoparticles. *J. Phys. Condens. Matter* 18 L179
[56] Qin Q., Xu F., Cao Y., Ro P. I. and Zhu Y. (2012) Measuring True Young's Modulus of a Cantilevered Nanowire: Effect of Clamping on Resonance Frequency. *Small* 8 2571–6
[57] Asthana A., Momeni K., Prasad A., Yap Y. K. and Yassar R. S. (2011) *In situ* observation of size-scale effects on the mechanical properties of ZnO nanowires. *Nanotechnology* 22 265712
[58] Akita S., Nishijima H., Kishida T. and Nakayama Y. (2000) Influence of Force Acting on Side Face of Carbon Nanotube in Atomic Force Microscopy. *Jpn. J. Appl. Phys.* 39 3724
[59] Tan E. P. S. and Lim C. T. (2006) Mechanical characterization of nanofibers – A review. *Compos. Sci. Technol.* 66 1102–11
[60] Zhu Y., Ke C. and Espinosa H. D. (2007) Experimental Techniques for the Mechanical Characterization of One-Dimensional Nanostructures. *Exp. Mech.* 47 7–24
[61] Chen Y., Dorgan B. L., McIlroy D. N. and Aston D. E. (2006) On the importance of boundary conditions on nanomechanical bending behavior and elastic modulus determination of silver nanowires. *J. Appl. Phys.* 100 104301
[62] Clifford C. A. and Seah M. P. (2005) The determination of atomic force microscope cantilever spring constants via dimensional methods for nanomechanical analysis. *Nanotechnology* 16 1666–80
[63] Burnham N. A., Chen X., Hodges C. S., Matei G. A., Thoreson E. J., Roberts C. J., Davies M. C. and Tendler S. J. B. (2002) Comparison of calibration methods for atomic-force microscopy cantilevers. *Nanotechnology* 14 1–6
[64] Timoshenko S. and Goodier J. N. (1951) *Theory of Elasticity*. New York, McGraw-Hill Book Company Inc.
[65] Zheng K., Wang C., Cheng Y.-Q., Yue Y., Han X., Zhang Z., Shan Z., Mao S. X., Ye M., Yin Y. and Ma E. (2010) Electron-beam-assisted superplastic shaping of nanoscale amorphous silica. *Nat. Commun.* 1 24
[66] Sheng H., Zheng H., Cao F., Wu S., Li L., Liu C., Zhao D. and Wang J. (2015) Anelasticity of twinned CuO nanowires. *Nano Res.* 8 3687–93
[67] Wang S., Wu Y., Lin L., He Y. and Huang H. (2015) Fracture Strain of SiC Nanowires and Direct Evidence of Electron-Beam Induced Amorphisation in the Strained Nanowires. *Small* 11 1672–6
[68] Kern P., Jäggi C., Utke I., Friedli V. and Michler J. (2006) Local electron beam induced reduction and crystallization of amorphous titania films. *Appl. Phys. Lett.* 89 021902
[69] Denisyuk A. I., Krasavin A. V., Komissarenko F. E. and Mukhin I. S. (2014) Mechanical, Electrostatic, and Electromagnetic Manipulation of Microobjects and Nanoobjects in Electron Microscopes. *Advances in Imaging and Electron Physics* 186 101–40
[70] Zhou P., Wu C. and Li X. (2008) Three-point bending Young's modulus of nanowires. *Meas. Sci. Technol.* 19 115703

[71] Zhang D., Breguet J.-M., Clavel R., Philippe L., Utke I. and Michler J. (2009) In situ tensile testing of individual Co nanowires inside a scanning electron microscope. *Nanotechnology* 20 365706
[72] Cleland A. N. (2003) *Foundations of Nanomechanics: From Solid-State Theory to Device Applications*. Berlin Heidelberg, Springer-Verlag)
[73] Tan E. P. S. and Lim C. T. (2006) Effects of annealing on the structural and mechanical properties of electrospun polymeric nanofibres. *Nanotechnology* 17 2649
[74] Barber A. H., Kaplan-Ashiri I., Cohen S. R., Tenne R. and Wagner H. D. (2005) Stochastic strength of nanotubes: An appraisal of available data. *Compos. Sci. Technol.* 65 2380–4
[75] He M.-R. and Zhu J. (2011) Defect-dominated diameter dependence of fracture strength in single-crystalline ZnO nanowires: In situ experiments. *Phys. Rev. B* 83 161302
[76] Duncan K. L., Wang Y., Bishop S. R., Ebrahimi F. and Wachsman E. D. (2006) Role of Point Defects in the Physical Properties of Fluorite Oxides. *J. Am. Ceram. Soc.* 89 3162–6
[77] Pan Y., Zheng W. T., Guan W. M., Zhang K. H., Yu S. S. and Hu X. Y. (2014) Effect of boron vacancies on mechanical properties of ReB2 from first-principles calculation. *Comput. Mater. Sci.* 82 12–6
[78] Vlassov S., Polyakov B., Dorogin L. M., Vahtrus M., Mets M., Antsov M., Saar R., Romanov A. E., Lõhmus A. and Lõhmus R. (2014) Shape Restoration Effect in Ag–SiO2 Core–Shell Nanowires. *Nano Lett.* 14 5201–5
[79] Khanal B. P., Pandey A., Li L., Lin Q., Bae W. K., Luo H., Klimov V. I. and Pietryga J. M. (2012) Generalized Synthesis of Hybrid Metal–Semiconductor Nanostructures Tunable from the Visible to the Infrared. *ACS Nano* 6 3832–40
[80] Ma J., Liu Y., Hao P., Wang J. and Zhang Y. (2016) Effect of different oxide thickness on the bending Young's modulus of SiO_2@SiC nanowires. *Sci. Rep.* 6 18994
[81] Aifantis K. E., Kolesnikova A. L. and Romanov A. E. (2007) Nucleation of misfit dislocations and plastic deformation in core/shell nanowires. *Philos. Mag.* 87 4731–57
[82] Liu X. W., Hu J. and Pan B. C. (2008) The composition-dependent mechanical properties of Ge/Si core–shell nanowires. *Phys. E Low-Dimens. Syst. Nanostructures* 40 3042–8
[83] Doebelin N. and Kleeberg R. (2015) Profex: a graphical user interface for the Rietveld refinement program BGMN. *J. Appl. Crystallogr.* 48 1573–80
[84] Bergmann J., Friedel P. and Kleeberg R. (1998) BGMN – A new fundamental parameters based Rietveld program for laboratory X-ray sources, it's use in quantitative analysis and structure investigations. *CPD Newsl.* 20 5–8
[85] Vlassov S., Polyakov B., Dorogin L. M., Lõhmus A., Romanov A. E., Kink I., Gnecco E. and Lõhmus R. (2011) Real-time manipulation of gold nanoparticles inside a scanning electron microscope. *Solid State Commun.* 151 688–92
[86] Rozhok S. and Chandrasekhar V. (2002) Application of commercially available cantilevers in tuning fork Scanning Probe Microscopy (SPM) studies. *Solid State Commun.* 121 683–6
[87] Vahtrus M., Umalas M., Polyakov B., Dorogin L., Saar R., Tamme M., Saal K., Lõhmus R. and Vlassov S. (2015) Mechanical and structural characterizations of gamma- and alpha-alumina nanofibers. *Mater. Charact.* 107 119–24

[88] Lu C. (2008) On the bending strength of ZnO nanowires. *Phys. Lett. A* 372 6113–5
[89] Landau L. D. and Lifshitz E. M. (1970) *Theory of Elasticity*. Oxford, Pergamon Press
[90] Heidelberg A., Ngo L. T., Wu B., Phillips M. A., Sharma S., Kamins T. I., Sader J. E. and Boland J. J. (2006) A Generalized Description of the Elastic Properties of Nanowires. *Nano Lett.* 6 1101–6
[91] Vahtrus M., Šutka A., Polyakov B., Oras S., Antsov M., Doebelin N., Lõhmus R., Nõmmiste E. and Vlassov S. (2016) Effect of cobalt doping on the mechanical properties of ZnO nanowires. *Mater. Charact.* 121 40–7
[92] Vlassov S., Polyakov B., Oras S., Vahtrus M., Antsov M., Šutka A., Smits K., Dorogin L. M. and Lõhmus R. (2016) Complex tribomechanical characterization of ZnO nanowires: nanomanipulations supported by FEM simulations. *Nanotechnology* 27 335701
[93] Persano L., Camposeo A., Tekmen C. and Pisignano D. (2013) Industrial Upscaling of Electrospinning and Applications of Polymer Nanofibers: A Review. *Macromol. Mater. Eng.* 298 504–20
[94] Orendorz A., Brodyanski A., Lösch J., Bai L. H., Chen Z. H., Le Y. K., Ziegler C. and Gnaser H. (2007) Phase transformation and particle growth in nanocrystalline anatase TiO2 films analyzed by X-ray diffraction and Raman spectroscopy. *Surf. Sci.* 601 4390–4
[95] Amin S. S., Li S., Wu X., Ding W. and Xu T. T. (2010) Facile Synthesis and Tensile Behavior of TiO 2 One-Dimensional Nanostructures. *Nanoscale Res. Lett.* 5 338
[96] Lee S.-H., Tekmen C. and Sigmund W. M. (2005) Three-point bending of electrospun TiO2 nanofibers. *Mater. Sci. Eng. A* 398 77–81
[97] Xu S., Li A., Poirier G. and Yao N. (2012) In Situ Mechanical and Electrical Characterization of Individual TiO2 Nanofibers Using a Nanomanipulator System. *Scanning* 34 341–6
[98] Lin T. (2011) *Nanofibers: Production, Properties and Functional Applications*. London, IntechOpen
[99] Wang C.-J., Huang C.-Y. and Wu Y.-C. (2009) Two-step sintering of fine alumina–zirconia ceramics. *Ceram. Int.* 35 1467–72
[100] Krenkel W. (2008) *Ceramic Matrix Composites: Fiber Reinforced Ceramics and their Applications*. Wiley
[101] Lee G. W. (2013) Phase transition characteristics of flame-synthesized gamma-Al2O3 nanoparticles with heat treatment. *Int J Chem Nucl Mater Met. Eng* 7 358–61
[102] Cava S., Tebcherani S. M., Souza I. A., Pianaro S. A., Paskocimas C. A., Longo E. and Varela J. A. (2007) Structural characterization of phase transition of Al2O3 nanopowders obtained by polymeric precursor method. *Mater. Chem. Phys.* 103 394–9
[103] Kim Y. A., Hayashi T., Endo M., Kaburagi Y., Tsukada T., Shan J., Osato K. and Tsuruoka S. (2005) Synthesis and structural characterization of thin multi-walled carbon nanotubes with a partially facetted cross section by a floating reactant method. *Carbon* 43 2243–50
[104] Yu P.-C., Yang R.-J., Tsai Y.-Y., Sigmund W. and Yen F.-S. (2011) Growth mechanism of single-crystal α-Al2O3 nanofibers fabricated by electrospinning techniques. *J. Eur. Ceram. Soc.* 31 723–31

[105] Zhao Z., Shen X., Yao H., Wang J., Chen J. and Li Z. (2014) Alumina nanofibers obtained via electrospinning of pseudo-boehmite sol/PVP solution. *J. Sol-Gel Sci. Technol.* 70 72–80
[106] Zhang P., Chen D. and Jiao X. (2012) Fabrication of Flexible α-Alumina Fibers Composed of Nanosheets. *Eur. J. Inorg. Chem.* 2012 4167–73
[107] Kuriakose S., Satpati B. and Mohapatra S. (2014) Enhanced photocatalytic activity of Co doped ZnO nanodisks and nanorods prepared by a facile wet chemical method. *Phys. Chem. Chem. Phys.* 16 12741–9
[108] Šutka A., Käämbre T., Pärna R., Juhnevica I., Maiorov M., Joost U. and Kisand V. (2016) Co doped ZnO nanowires as visible light photocatalysts. *Solid State Sci.* 56 54–62
[109] Huang Y., Zhang Y., Wang X., Bai X., Gu Y., Yan X., Liao Q., Qi J. and Liu J. (2009) Size Independence and Doping Dependence of Bending Modulus in ZnO Nanowires. *Cryst. Growth Des.* 9 1640–2
[110] Chen C. Q. and Zhu J. (2007) Bending strength and flexibility of ZnO nanowires. *Appl. Phys. Lett.* 90 043105
[111] Hirth J. P. and Lothe J. (1982) *Theory of Dislocations*. New York, Wiley
[112] Moon H., Lee H., Kwon J., Suh Y. D., Kim D. K., Ha I., Yeo J., Hong S. and Ko S. H. (2017) Ag/Au/Polypyrrole Core-shell Nanowire Network for Transparent, Stretchable and Flexible Supercapacitor in Wearable Energy Devices. *Sci. Rep.* 7 41981
[113] Larki P., Sabri Y. M., Kabir K. M. M., Nafady A., Kandjani A. E. and Bhargava S. K. (2015) Silver/gold core/shell nanowire monolayer on a QCM microsensor for enhanced mercury detection. *RSC Adv.* 5 92303–11
[114] Tripp M. K., Stampfer C., Miller D. C., Helbling T., Herrmann C. F., Hierold C., Gall K., George S. M. and Bright V. M. (2006) The mechanical properties of atomic layer deposited alumina for use in micro- and nano-electromechanical systems. *Sens. Actuators Phys.* 130–131 419–29
[115] Peng P., Liu L., Gerlich A. P., Hu A. and Zhou Y. N. (2013) Self-Oriented Nanojoining of Silver Nanowires via Surface Selective Activation. *Part. Part. Syst. Charact.* 30 420–6
[116] Pelleg J. (2013) *Mechanical Properties of Materials*. Netherlands, Springer

PUBLICATIONS

CURRICULUM VITAE

Name Mikk Vahtrus
Date of birth November 23, 1989
Citizenship Estonian
Telephone +372 5562 1524
E-mail mikk.vahtrus@ut.ee

Education

2014–2018	University of Tartu, PhD in Physics
2012–2014	University of Tartu, MSc in Physics (*cum laude*)
2008–2011	University of Tartu, BSc in Physics
2001–2008	Tallinn Sikupilli Secondary School (graduated with silver medal)
1997–2001	Aakre Elementary School

Professional experience

2018–	Estonian Research Council, Research Funding Officer
2016–2018	University of Tartu, Institute of Physics, Junior Research Fellow
2015	Estonian Nanotechnology Competence Center, technical staff
2014–2015	University of Tartu, Institute of Physics, laboratory assistant

Awards

2014	University of Tartu, Institute of Physics, student award

Main research area
Characterization of one-dimensional nanostructures

ELULOOKIRJELDUS

Nimi	Mikk Vahtrus
Sünniaeg	23. november 1989
Kodakondsus	Eesti
Telefon	+372 5562 1524
E-mail	mikk.vahtrus@ut.ee

Haridus

2014–2018	Tartu Ülikool, doktoriõpe füüsika erialal
2012–2014	Tartu Ülikool, magistriõpe füüsika erialal (lõpetanud *cum laude*)
2008–2011	Tartu Ülikool, bakalaureuseõpe füüsika erialal
2001–2008	Tallinna Sikupilli Keskkool (lõpetanud hõbemedaliga)
1997–2001	Aakre algkool

Töökogemus

2018-	Sihtasutus Eesti Teadusagentuur, uurimistoetuste koordinaator
2016–2018	Tartu Ülikool, Füüsika Instituut, nooremteadur
2015	Eesti Nanotehnoloogia Arenduskeskus, tehniline töötaja
2014–2015	Tartu Ülikool, Füüsika Instituut, laborant

Auhinnad

2014	Tartu Ülikool, Füüsika Instituut, tudengistipendium

Peamine uurimisvaldkond

Ühedimensionaalsete nanostruktuuride karakteriseerimine.

DISSERTATIONES PHYSICAE UNIVERSITATIS TARTUENSIS

1. **Andrus Ausmees.** XUV-induced electron emission and electron-phonon interaction in alkali halides. Tartu, 1991.
2. **Heiki Sõnajalg.** Shaping and recalling of light pulses by optical elements based on spectral hole burning. Tartu, 1991.
3. **Sergei Savihhin.** Ultrafast dynamics of F-centers and bound excitons from picosecond spectroscopy data. Tartu, 1991.
4. **Ergo Nõmmiste.** Leelishalogeniidide röntgenelektronemissioon kiiritamisel footonitega energiaga 70–140 eV. Tartu, 1991.
5. **Margus Rätsep.** Spectral gratings and their relaxation in some low-temperature impurity-doped glasses and crystals. Tartu, 1991.
6. **Tõnu Pullerits.** Primary energy transfer in photosynthesis. Model calculations. Tartu, 1991.
7. **Olev Saks.** Attoampri diapasoonis voolude mõõtmise füüsikalised alused. Tartu, 1991.
8. **Andres Virro.** AlGaAsSb/GaSb heterostructure injection lasers. Tartu, 1991.
9. **Hans Korge.** Investigation of negative point discharge in pure nitrogen at atmospheric pressure. Tartu, 1992.
10. **Jüri Maksimov.** Nonlinear generation of laser VUV radiation for high-resolution spectroscopy. Tartu, 1992.
11. **Mark Aizengendler.** Photostimulated transformation of aggregate defects and spectral hole burning in a neutron-irradiated sapphire. Tartu, 1992.
12. **Hele Siimon.** Atomic layer molecular beam epitaxy of A^2B^6 compounds described on the basis of kinetic equations model. Tartu, 1992.
13. **Tõnu Reinot.** The kinetics of polariton luminescence, energy transfer and relaxation in anthracene. Tartu, 1992.
14. **Toomas Rõõm.** Paramagnetic H^{2-} and F^+ centers in CaO crystals: spectra, relaxation and recombination luminescence. Tallinn, 1993.
15. **Erko Jalviste.** Laser spectroscopy of some jet-cooled organic molecules. Tartu, 1993.
16. **Alvo Aabloo.** Studies of crystalline celluloses using potential energy calculations. Tartu, 1994.
17. **Peeter Paris.** Initiation of corona pulses. Tartu, 1994.
18. **Павел Рубин.** Локальные дефектные состояния в CuO_2 плоскостях высокотемпературных сверхпроводников. Тарту, 1994.
19. **Olavi Ollikainen.** Applications of persistent spectral hole burning in ultrafast optical neural networks, time-resolved spectroscopy and holographic interferometry. Tartu, 1996.
20. **Ülo Mets.** Methodological aspects of fluorescence correlation spectroscopy. Tartu, 1996.
21. **Mikhail Danilkin.** Interaction of intrinsic and impurity defects in CaS:Eu luminophors. Tartu, 1997.

22. **Ирина Кудрявцева.** Создание и стабилизация дефектов в кристаллах KBr, KCl, RbCl при облучении ВУФ-радиацией. Тарту, 1997.
23. **Andres Osvet.** Photochromic properties of radiation-induced defects in diamond. Tartu, 1998.
24. **Jüri Örd.** Classical and quantum aspects of geodesic multiplication. Tartu, 1998.
25. **Priit Sarv.** High resolution solid-state NMR studies of zeolites. Tartu, 1998.
26. **Сергей Долгов.** Электронные возбуждения и дефектообразование в некоторых оксидах металлов. Тарту, 1998.
27. **Kaupo Kukli.** Atomic layer deposition of artificially structured dielectric materials. Tartu, 1999.
28. **Ivo Heinmaa.** Nuclear resonance studies of local structure in $RBa_2Cu_3O_{6+x}$ compounds. Tartu, 1999.
29. **Aleksander Shelkan.** Hole states in CuO_2 planes of high temperature superconducting materials. Tartu, 1999.
30. **Dmitri Nevedrov.** Nonlinear effects in quantum lattices. Tartu, 1999.
31. **Rein Ruus.** Collapse of 3d (4f) orbitals in 2p (3d) excited configurations and its effect on the x-ray and electron spectra. Tartu, 1999.
32. **Valter Zazubovich.** Local relaxation in incommensurate and glassy solids studied by Spectral Hole Burning. Tartu, 1999.
33. **Indrek Reimand.** Picosecond dynamics of optical excitations in GaAs and other excitonic systems. Tartu, 2000.
34. **Vladimir Babin.** Spectroscopy of exciton states in some halide macro- and nanocrystals. Tartu, 2001.
35. **Toomas Plank.** Positive corona at combined DC and AC voltage. Tartu, 2001.
36. **Kristjan Leiger.** Pressure-induced effects in inhomogeneous spectra of doped solids. Tartu, 2002.
37. **Helle Kaasik.** Nonperturbative theory of multiphonon vibrational relaxation and nonradiative transitions. Tartu, 2002.
38. **Tõnu Laas.** Propagation of waves in curved spacetimes. Tartu, 2002.
39. **Rünno Lõhmus.** Application of novel hybrid methods in SPM studies of nanostructural materials. Tartu, 2002.
40. **Kaido Reivelt.** Optical implementation of propagation-invariant pulsed free-space wave fields. Tartu, 2003.
41. **Heiki Kasemägi.** The effect of nanoparticle additives on lithium-ion mobility in a polymer electrolyte. Tartu, 2003.
42. **Villu Repän.** Low current mode of negative corona. Tartu, 2004.
43. **Алексей Котлов.** Оксианионные диэлектрические кристаллы: зонная структура и электронные возбуждения. Tartu, 2004.
44. **Jaak Talts.** Continuous non-invasive blood pressure measurement: comparative and methodological studies of the differential servo-oscillometric method. Tartu, 2004.
45. **Margus Saal.** Studies of pre-big bang and braneworld cosmology. Tartu, 2004.

46. **Eduard Gerškevitš.** Dose to bone marrow and leukaemia risk in external beam radiotherapy of prostate cancer. Tartu, 2005.
47. **Sergey Shchemelyov.** Sum-frequency generation and multiphoton ionization in xenon under excitation by conical laser beams. Tartu, 2006.
48. **Valter Kiisk.** Optical investigation of metal-oxide thin films. Tartu, 2006.
49. **Jaan Aarik.** Atomic layer deposition of titanium, zirconium and hafnium dioxides: growth mechanisms and properties of thin films. Tartu, 2007.
50. **Astrid Rekker.** Colored-noise-controlled anomalous transport and phase transitions in complex systems. Tartu, 2007.
51. **Andres Punning.** Electromechanical characterization of ionic polymer-metal composite sensing actuators. Tartu, 2007.
52. **Indrek Jõgi.** Conduction mechanisms in thin atomic layer deposited films containing TiO_2. Tartu, 2007.
53. **Aleksei Krasnikov.** Luminescence and defects creation processes in lead tungstate crystals. Tartu, 2007.
54. **Küllike Rägo.** Superconducting properties of MgB_2 in a scenario with intra- and interband pairing channels. Tartu, 2008.
55. **Els Heinsalu.** Normal and anomalously slow diffusion under external fields. Tartu, 2008.
56. **Kuno Kooser.** Soft x-ray induced radiative and nonradiative core-hole decay processes in thin films and solids. Tartu, 2008.
57. **Vadim Boltrushko.** Theory of vibronic transitions with strong nonlinear vibronic interaction in solids. Tartu, 2008.
58. **Andi Hektor.** Neutrino Physics beyond the Standard Model. Tartu, 2008.
59. **Raavo Josepson.** Photoinduced field-assisted electron emission into gases. Tartu, 2008.
60. **Martti Pärs.** Study of spontaneous and photoinduced processes in molecular solids using high-resolution optical spectroscopy. Tartu, 2008.
61. **Kristjan Kannike.** Implications of neutrino masses. Tartu, 2008.
62. **Vigen Issahhanjan.** Hole and interstitial centres in radiation-resistant MgO single crystals. Tartu, 2008.
63. **Veera Krasnenko.** Computational modeling of fluorescent proteins. Tartu, 2008.
64. **Mait Müntel.** Detection of doubly charged higgs boson in the CMS detector. Tartu, 2008.
65. **Kalle Kepler.** Optimisation of patient doses and image quality in diagnostic radiology. Tartu, 2009.
66. **Jüri Raud.** Study of negative glow and positive column regions of capillary HF discharge. Tartu, 2009.
67. **Sven Lange.** Spectroscopic and phase-stabilisation properties of pure and rare-earth ions activated ZrO_2 and HfO_2. Tartu, 2010.
68. **Aarne Kasikov.** Optical characterization of inhomogeneous thin films. Tartu, 2010.
69. **Heli Valtna-Lukner.** Superluminally propagating localized optical pulses. Tartu, 2010.

70. **Artjom Vargunin.** Stochastic and deterministic features of ordering in the systems with a phase transition. Tartu, 2010.
71. **Hannes Liivat.** Probing new physics in e+e− annihilations into heavy particles via spin orientation effects. Tartu, 2010.
72. **Tanel Mullari.** On the second order relativistic deviation equation and its applications. Tartu, 2010.
73. **Aleksandr Lissovski.** Pulsed high-pressure discharge in argon: spectroscopic diagnostics, modeling and development. Tartu, 2010.
74. **Aile Tamm.** Atomic layer deposition of high-permittivity insulators from cyclopentadienyl-based precursors. Tartu, 2010.
75. **Janek Uin.** Electrical separation for generating standard aerosols in a wide particle size range. Tartu, 2011.
76. **Svetlana Ganina.** Hajusandmetega ülesanded kui üks võimalus füüsikaõppe efektiivsuse tõstmiseks. Tartu, 2011
77. **Joel Kuusk.** Measurement of top-of-canopy spectral reflectance of forests for developing vegetation radiative transfer models. Tartu, 2011.
78. **Raul Rammula**. Atomic layer deposition of HfO_2 – nucleation, growth and structure development of thin films. Tartu, 2011.
79. **Сергей Наконечный.** Исследование электронно-дырочных и интерстициал-вакансионных процессов в монокристаллах MgO и LiF методами термоактивационной спектроскопии. Тарту, 2011.
80. **Niina Voropajeva.** Elementary excitations near the boundary of a strongly correlated crystal. Tartu, 2011.
81. **Martin Timusk.** Development and characterization of hybrid electro-optical materials. Tartu, 2012, 106 p.
82. **Merle Lust.** Assessment of dose components to Estonian population. Tartu, 2012, 84 p.
83. **Karl Kruusamäe.** Deformation-dependent electrode impedance of ionic electromechanically active polymers. Tartu, 2012, 128 p.
84. **Liis Rebane.** Measurement of the $W \to \tau\nu$ cross section and a search for a doubly charged Higgs boson decaying to τ-leptons with the CMS detector. Tartu, 2012, 156 p.
85. **Jevgeni Šablonin.** Processes of structural defect creation in pure and doped MgO and NaCl single crystals under condition of low or super high density of electronic excitations. Tartu, 2013, 145 p.
86. **Riho Vendt**. Combined method for establishment and dissemination of the international temperature scale. Tartu, 2013, 108 p.
87. **Peeter Piksarv.** Spatiotemporal characterization of diffractive and non-diffractive light pulses. Tartu, 2013, 156 p.
88. **Anna Šugai.** Creation of structural defects under superhigh-dense irradiation of wide-gap metal oxides. Tartu, 2013, 108 p.
89. **Ivar Kuusik.** Soft X-ray spectroscopy of insulators. Tartu, 2013, 113 p.
90. **Viktor Vabson**. Measurement uncertainty in Estonian Standard Laboratory for Mass. Tartu, 2013, 134 p.

91. **Kaupo Voormansik.** X-band synthetic aperture radar applications for environmental monitoring. Tartu, 2014, 117 p.
92. **Deivid Pugal.** hp-FEM model of IPMC deformation. Tartu, 2014, 143 p.
93. **Siim Pikker.** Modification in the emission and spectral shape of photostable fluorophores by nanometallic structures. Tartu, 2014, 98 p.
94. **Mihkel Pajusalu**. Localized Photosynthetic Excitons. Tartu, 2014, 183 p.
95. **Taavi Vaikjärv.** Consideration of non-adiabaticity of the Pseudo-Jahn-Teller effect: contribution of phonons. Tartu, 2014, 129 p.
96. **Martin Vilbaste.** Uncertainty sources and analysis methods in realizing SI units of air humidity in Estonia. Tartu, 2014, 111 p.
97. **Mihkel Rähn.** Experimental nanophotonics: single-photon sources- and nanofiber-related studies. Tartu, 2015, 107 p.
98. **Raul Laasner.** Excited state dynamics under high excitation densities in tungstates. Tartu, 2015, 125 p.
99. **Andris Slavinskis.** EST Cube-1 attitude determination. Tartu, 2015, 104 p.
100. **Karlis Zalite**. Radar Remote Sensing for Monitoring Forest Floods and Agricultural Grasslands. Tartu, 2016, 124 p.
101. **Kaarel Piip.** Development of LIBS for *in-situ* study of ITER relevant materials. Tartu, 2016, 93 p.
102. **Kadri Isakar.** ^{210}Pb in Estonian air: long term study of activity concentrations and origin of radioactive lead. Tartu, 2016, 107 p.
103. **Artur Tamm.** High entropy alloys: study of structural properties and irradiation response. Tartu, 2016, 115 p.
104. **Rasmus Talviste.** Atmospheric-pressure He plasma jet: effect of dielectric tube diameter. Tartu, 2016, 107 p.
105. **Andres Tiko.** Measurement of single top quark properties with the CMS detector. Tartu, 2016, 161 p.
106. **Aire Olesk.** Hemiboreal Forest Mapping with Interferometric Synthetic Aperture Radar. Tartu, 2016, 121 p.
107. **Fred Valk.** Nitrogen emission spectrum as a measure of electric field strength in low-temperature gas discharges. Tartu, 2016, 149 p.
108. **Manoop Chenchiliyan.** Nano-structural Constraints for the Picosecond Excitation Energy Migration and Trapping in Photosynthetic Membranes of Bacteria. Tartu, 2016, 115p.
109. **Lauri Kaldamäe.** Fermion mass and spin polarisation effects in top quark pair production and the decay of the higgs boson. Tartu, 2017, 104 p.
110. **Marek Oja.** Investigation of nano-size α- and transition alumina by means of VUV and cathodoluminescence spectroscopy. Tartu, 2017, 89 p.
111. **Viktoriia Levushkina.** Energy transfer processes in the solid solutions of complex oxides. Tartu, 2017, 101 p.
112. **Mikk Antsov.** Tribomechanical properties of individual 1D nanostructures: experimental measurements supported by finite element method simulations. Tartu, 2017, 101 p.
113. **Hardi Veermäe.** Dark matter with long range vector-mediated interactions. Tartu, 2017, 137 p.

114. **Aris Auzans.** Development of computational model for nuclear energy systems analysis: natural resources optimisation and radiological impact minimization. Tartu, 2018, 138 p.
115. **Aleksandr Gurev**. Coherent fluctuating nephelometry application in laboratory practice. Tartu, 2018, 150 p.
116. **Ardi Loot**. Enhanced spontaneous parametric downconversion in plasmonic and dielectric structures. Tartu, 2018, 164 p.
117. **Andreas Valdmann.** Generation and characterization of accelerating light pulses. Tartu, 2019, 85 p.